M 2017

U.PORTO
FEUP FACULDADE DE ENGENHARIA
UNIVERSIDADE DO PORTO

THE APPLICATION OF IRON BASED METAL ORGANIC FRAMEWORKS AS SUPERCAPACITOR ELECTRODE MATERIALS

RAHUL FILIPE HONAVAR MELO PIRES

DISSERTAÇÃO DE MESTRADO APRESENTADA
À FACULDADE DE ENGENHARIA DA UNIVERSIDADE DO PORTO EM
ÁREA CIENTÍFICA

Master in Chemical Engineering

The Application of Iron Based Metal Organic Frameworks as Supercapacitor Electrode Materials

A Master's dissertation

of

Rahul Filipe Honavar Melo Pires

Developed within the course of dissertation

held in

National Taiwan University – Energy Materials Laboratory

Supervisor at NTU: **Professor Nae-Lih Wu**

U.PORTO
FEUP FACULDADE DE ENGENHARIA
UNIVERSIDADE DO PORTO

Departamento de Engenharia Química

August of 2017

Acknowledgments

To Professor Nae-Lih Wu for kindly giving me the opportunity to work in his laboratory under his supervision and giving a direction to the project.

To Mozaffar Abdollahifar for guiding me throughout the whole process and for introducing me to the techniques involved in the experiments.

To all my colleagues in the EML for the advice given and knowledge transmitted during the time spent working in the lab.

To Professor Madeira, Dcoop and OIA for making the exchange between universities possible.

To my family and friends for the support.

Thank you!

Abstract

Metal-organic frameworks (MOFs) are a versatile class of crystalline materials with varied applications as a result of their controllable structure, tunable pore size and large surface area. MOFs were synthesized from ferrous precursors and with 2-methylimidazole and 1,2,4-triazole as organic linkers to be used as supercapacitor electrode materials. In addition to attempting to reproduce synthesis of ZIF-8 in aqueous medium, three new materials were synthesized by a solvothermal process: Fe-MeIm-ST1, Fe-MeIm-ST2 and Fe-Trz-ST1. Materials were characterized using X-ray diffraction analysis, scanning electron microscopy, energy dispersive X-ray spectroscopy, transmission electron microscopy, nitrogen adsorption and electrochemical tests both before and after calcination. These were found to contain iron oxides. Of the three new materials synthesized, the specific capacitance of Fe-MeIm-ST2-V300, obtained from calcination of Fe-MeIm-ST2, was the highest (157 F/g), when sodium sulfite was used as an electrolyte, suggesting a possible application as a supercapacitor electrode material. However there is a need for further modification to increase stability and capacitance. The other materials produced, in their present form, did not have high capacitance.

Keywords (theme): MOFs; Solvothermal; Supercapacitor; 2-Methylimidazole; 1,2,4-Triazole

Declaration

I hereby declare, on my word of honour, that this work is original and that all non-original contributions were properly referenced with source identification.

Sign and date

Index

Notation and Glossary

C	Capacitance	F
A	Area of the plates	m^2
d	Separation of plates	m
E	Energy	J
V	Potential Difference	V
C_{avg}	Specific Capacitance	F/g
I_{avg}	Average of anodic and cathodic currents	A
s	Potential scan rate	V/s
w	Mass of the active material in the electrode	g
P	Pressure of adsorbed gas	
P_0	Saturate vapor pressure	
V	Volume of adsorbed nitrogen	cm^3/g
V_m	Volume if mono-layer adsorbed nitrogen	cm^3/g
c	BET constant	

Greek Letters

ε_r	Relative permittivity in the double layer
ε_0	Permittivity of free space
λ	Wavelength

List of Acronyms

EDLC	Electric Double Layer Capacitor
CV	Cyclic Voltammetry
MOF	Metal-Organic Framework
H_4DOBDC	2,5-dihydroxybenzene-1,4-dicarboxylic acid
DMF	N,N-dimethylformamide
H_4DSBDC	2,5-disulfhydrylbenzene-1,4-dicarboxylicacid
H_2BTDD	bis(1H-1,2,3-triazolo[4,5-b],[4,'5'-i]dibenzo[1,4]dioxin
ZIF	Zeolitic Imidazolate Framework
XRD	X-ray Diffraction
SEM	Scanning electron microscope
TEM	Transmission electron microscope
EDX	Energy dispersive X-ray spectroscopy
TGA	Thermogravimetric analysis
MeIm	2-Methylimidazole
Trz	1,2,4-Triazole
PVDF	Polyvinylidene difluoride
NMP	N-methylpyrrolidone

1 Introduction

This chapter describes what motivates current research for new Supercapacitor materials and has a brief presentation of the work performed for this dissertation.

1.1 Framing and presentation of the work

As society moves from the dependence on fossil fuels, due to its finite sources, increasing costs, pollution and geopolitical problems, towards renewable energy sources there is a high demand for energy storage devices and in particular, those with high power density and high energy density. The intermittent nature of renewable energy source and the need for high power from wind and solar sources can be solved by energy storage systems. Other applications include energy storage for small electronic devices and dynamic braking in transport systems [1].

Energy storage devices convert energy from one form into a form that can be stored in different mediums and then converted back into electrical energy when required [2]. Modern day life uses energy for a vast array of applications and this energy is provided by batteries, electrolytic capacitors, fuel cells and supercapacitors, all of which are energy storage devices, but with different electrochemical processes [3].

A Supercapacitor consists of two electrodes in an electrolyte with an ion permeable separator between them. Supercapacitors provide rapid power delivery and recharging however they have low energy density. Due to their highly reversible charge-storage process, supercapacitors have longer cycle-lives than batteries and higher charge and discharge rates at power rates exceeding 1 kW kg^{-1}. A further advantage is that high power performance can be achieved at temperatures as low as -40 °C [4] [5].

The supercapacitor can be classified in two different storage systems, the Electric Double Layer Capacitor (EDLC) and the pseudocapacitor. EDLCs are built from nano-scale materials which have a high porosity and high surface area, the capacitance results from an electrostatic accumulation of surface charge, no redox reactions are needed so there is a faster response to a change in potential. The pseudocapacitors have redox reactions during the charge and discharge processes, similar to batteries. A hybrid supercapacitor takes use of both faradaic and EDLC storage systems [6].

Most supercapacitor electrodes manufactured are made from carbon-based materials, metal oxides and conducting polymers. Carbon based materials are currently most commonly used, due to their unique chemical and physical properties, namely high conductivity, surface

area, good corrosion resistance, high temperature stability, controlled pore structure, processability and compatibily in composite materials [5]. In addition their cheap price and established production processes make them more accessible [1], [6]. Carbon materials currently used are activated carbons, carbide derived carbons, carbon nano-tubes, graphene and mesoporous carbons [1].

Metal organic frameworks (MOFs) first defined by Yaghi and Hailian are a class of crystalline porous materials which are made up from metal-containing units and organic linkers [7]. Their importance arises from their ability to reversibly bind molecules and ions within their channels [8]. By varying the metal containing units and characteristics of the organic linkers, different MOFs can be created. These materials have gained interest during the past two decades because of their high surface area, controllable structures and tunable pore size [8]. Their applications in gas storage and separation, sensors, catalysis, drug delivery and electrochemical systems are being explored [8] [9].

1.2 Aim

The main objective of this dissertation project was to produce a MOF with Iron containing units and to test its applicability as an electrode material for supercapacitors. In order to do this, the process of solvothermal synthesis with methanol was utilized.

The materials synthesized were characterized with X-ray diffraction, scanning electron microscopy, transmission electron microscopy, energy dispersive X-ray spectroscopy and thermogravimetric analysis and finally electrochemically tested.

1.3 Energy Materials Laboratory

The Energy Materials Laboratory where this work was carried out is located in the Chemical Engineering Department of the National Taiwan University, Taipei, Taiwan. The research interest of the laboratory is in the electrochemical field, focused on but not limited to Lithium-ion batteries and Supercapacitors. Researchers at the Energy Materials Laboratory consist of group leader Professor Nae-Lih Wu, 2 post doctorate researchers, 2 PhD students, and several masters and undergraduate students. The laboratory cooperates with institutes including the Industrial Technology Research Institute and the National Science Council of Taiwan.

1.4 Contributions of the Work

The objective of this dissertation is to create new materials which can be used as electrodes for supercapacitors. During the time I spent at the Energy Materials Laboratory I have applied solvothermal and hydrothermal methods for making MOFs, in attempting to create new MOFs and testing their electrochemical performance and to assess their potential supercapacitor applicability, using pre-existing methods already developed in the Laboratory which include the three electrode test for cyclic voltammetry and galvanostatic charge and discharge tests.

1.5 Organization of the thesis

The Thesis is divided into six chapters: Introduction, State of the Art, Materials and Methods, Results and Discussion and Conclusions.

Chapter 1: In the Introduction a brief description is given of the context, scope and significance of energy storage devices.

Chapter 2: The State of the Art covers the different covers basic concepts about supercapacitors and Metal Organic Frameworks which are relevant to this work.

Chapter 3: Methods and Materials describes the materials, including chemicals used and all the experimental procedures performed.

Chapter 4: In the Results and Discussion, all of the obtained results of the characterization tests and electrochemical tests are presented and discussed.

Chapter 5: In Conclusions and Future Perspectives, a summary of the results and their interpretation is given along with suggestions for further projects to modify the characteristics of the electrode material.

2 State of the Art

This chapter will go through a few basic concepts of the Supercapacitor and Metal Organic Frameworks.

2.1 Classification of Energy Storage Devices and Supercapacitors

The battery is regarded as the primary energy storage device and consists of an electrochemical cell which produce electricity with a desired voltage from an electrochemical reaction. Each cell contains two electrodes, the anode which is the negative electrode and the cathode, the positive electrode with an electrolyte which can be in liquid or solid state. A cell can bi-directionally convert energy between electrical and chemical energy. The charge storage mechanism is through bulk mass transfer between electrodes during both charge and discharge. During discharging, the electrochemical reactions occur at the anodes and the cathodes simultaneously. To the external circuit, electrons are provided from the anode and are collected at the cathode. The advantage of the battery is that it has high energy capacity and even energy discharge. Disadvantages include incapacity to bear high power delivery and lengthy recharging times. Careful disposal of batteries is required as most contain toxic materials [3] [10].

A fuel cell is an electrochemical cell which derives its energy from combustible substances for example hydrogen and methanol [10].

The electrolytic capacitor consists of two electrical conductors separated by a thin insulator called a dielectric. During charging, energy is stored in the dielectric material in an electrostatic field [2] [11]. Because of its small size and low capacitance, it is used in integrated chips and transistors.

The supercapacitor is a category of energy storage device. Composed of two electrodes, an electrolyte and a separator that electrically isolates the two electrodes. The electrode materials have a combination of physical and chemical properties, high conductivity, high surface area, controlled pore structure, good corrosion resistance and high temperature stability [5].

In an EDLC, when a voltage is applied, charges are electrostatically separated and an electric double layer is formed at the interface of the electrode and electrolyte. In the double layer capacitance is created when an excess of electric charges accumulates at the electrode surface, on the electrolyte side opposite charged ions counterbalance at the surface to reach electroneutrality. Within the electrolyte, cations move towards the negative electrode and

anions towards the positive electrode. During discharge, this process is reversed. A diagram of an EDLC is displayed in Figure 1. The corresponding capacitance formed at the interface is expressed by eq. (1).

$$C = \frac{A\varepsilon_r\varepsilon_0}{d} \quad (1)$$

The double layer is formed from ions or solvated ions. The layer formed will have a thickness, estimated as 5-10 Å for concentrated electrolytes, dependent on the size of the ions. The capacitance of the electrode is further increased by using porous electrodes with a high internal surface area. [12]

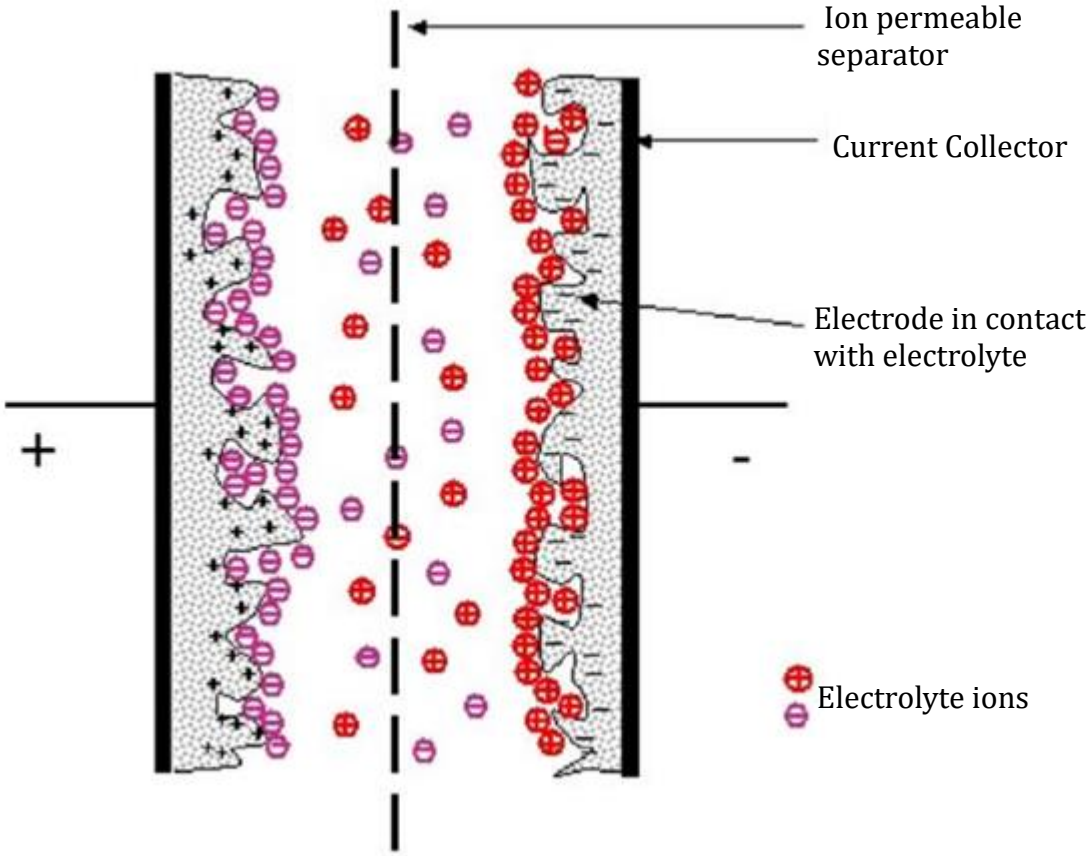

Figure 1 – Diagram of an EDLC (adapted from Pandolfo & Hollenkamp, 2006) [5]

If an electrolyte can sustain a higher operation voltage, more energy can be stored since the energy in a capacitor is proportional to the voltage squared (eq. (2)).

$$E = \frac{1}{2} CV^2 \quad (2)$$

When applying a potential on a faradaic supercapacitor also known as a pseudocapacitor, fast and reversible reactions are taking place on the electrode materials, from faradaic current passing through the supercapacitor cell similar to the charge-discharge process of a battery. Materials which are used as pseudocapacitor electrodes are metal oxides and conducting polymers. Faradaic processes which occur in electrodes are reversible adsorption, redox reactions of transition metal oxides and reversible doping on conductive polymers. The faradaic supercapacitor can have a capacitance 10-100 times higher than the electrostatic capacitance of an EDLC but have lower power density because faradaic processes are slower, it also lacks stability during cycling due to reactions occurring at the electrode [1] [13].

The Supercapacitor has a specific energy of several orders higher than conventional capacitor and a specific power higher than most batteries, which has been represented on a Ragone plot, comparing the performance of various energy storage devices (Figure 2). Filling this gap, supercapacitors have been useful in complementing the shortcomings of batteries and fuel cells because of their longer cycle-lives and ability to charge and discharge at power densities exceeding 1 kW kg^{-1}. These properties allow for applications such as consumer electronics, hybrid vehicles and industrial power management [5].

The supercapacitor is limited by its energy density of about 5 W h kg^{-1} which is much lower than that achieved by batteries. When an application of higher energy capacity is required, a much larger supercapacitor is needed which increases manufacturing costs. [14]

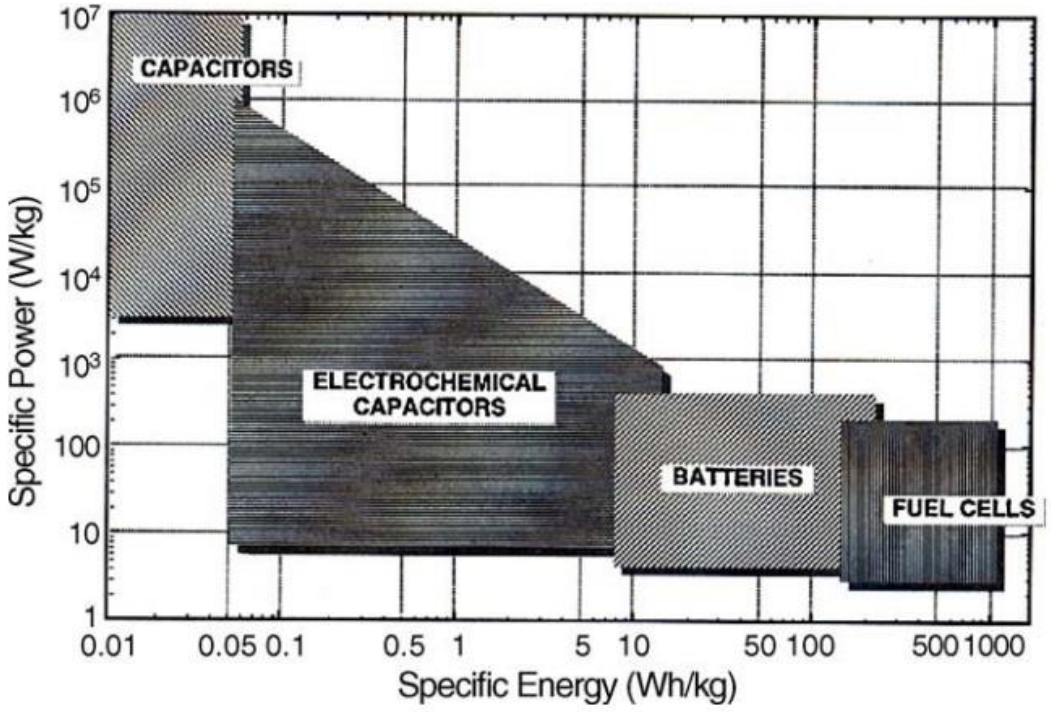

Figure 2- Specific energy and power capabilities of capacitors (electrostatic), electrochemical capacitors (supercapacitors), batteries and fuel cells [14].

2.2 Electrode Materials

Capacitance of the supercapacitor depends on the materials used for the electrode, it is dependent on the specific surface area of the electrode materials but only the area which is accessible to the electrolyte.

The pore size and pore distribution of the material also play a role in the performance of the electrode, energy density increases with increasing cell voltage but saturates at higher voltages when pores are not able to accommodate the additional charge and therefore are unable to accommodate more energy. Figure 3 displays a contour plot of energy density *E* as a function of working voltage (*V*) and the pore width (*nm*), the highest energy density is observed at high operating densities and bigger pores. Narrowing the pore size distribution increases the stored energy density, a monodisperse porous electrode would be ideal for energy storage. [15]

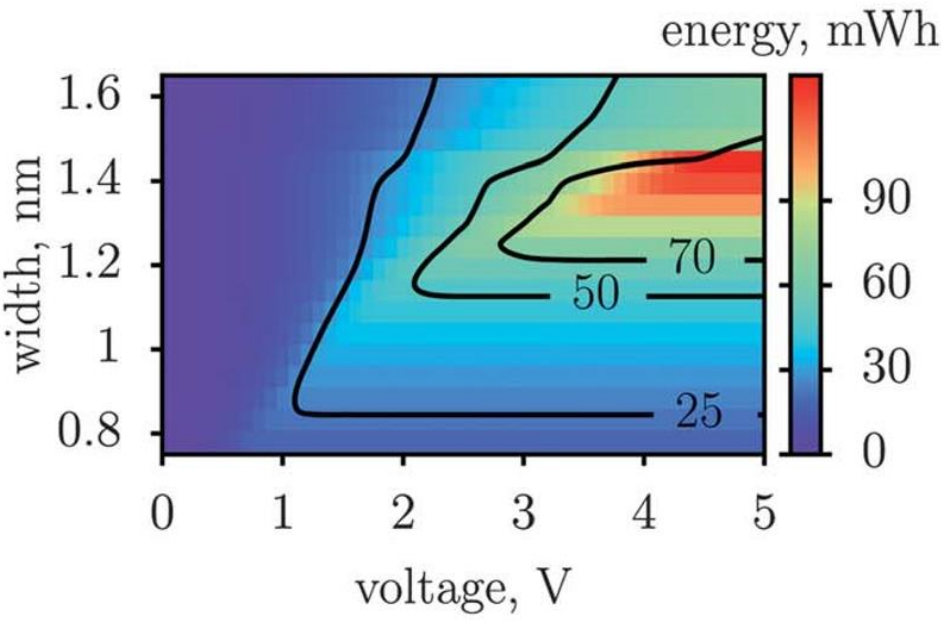

Figure 3 – Contour plot of the stored energy density E (mW.h/c^{-3}) spanned in the pore width/working voltage plane. [15]

2.3 Metal-organic framework

Metal-organic frameworks (MOFs) are a class of porous materials made up of metal containing units and organic linkers. Advantages of MOFs over carbon based materials is their high porosity and controllable structure and tunable pore size. By varying metal units or synthesis conditions, MOFs of different functionalities can be created. Over 20,000 MOFs have been created with increasing possibilities to create new materials. These materials are used for gas storage and separation, sensor, catalysis, drug delivery and in electrochemical systems [8] [9].

MOFs can be applied as supercapacitor materials in different ways, pristine MOFs can store charge through the adsorption of electrolyte ions on their internal surface or by reversible redox reactions with the metal centers, the MOFs can be destroyed to obtain metal oxides or pyrolyzed to give porous carbons.

The majority of MOFs exhibit a low electrical conductivity, as a consequence of redox-inactive organic ligands bound to metal ions via oxygen or nitrogen atoms. [16] MOFs containing Fe^{2+} ions have exhibited electrical conductivity of at least 5 orders of magnitude higher compared to Mg, Mn, Co, Ni, Cu, Zn and Cd ions using four different organic ligands. The four families of MOFs tested in Sun *et. al.* (2017) were $M_2(DOBDC)(DMF)_2$ (M = Mg^{2+}, Mn^{2+}, Fe^{2+}, Co^{2+}, Ni^{2+}, Cu^{2+}, Zn^{2+}; H_4DOBDC = 2,5-dihydroxybenzene-1,4-dicarboxylic acid;

DMF = N,N-dimethylformamide), $M_2(DSBDC)(DMF)_2$ (M = Mn^{2+}, Fe^{2+}; H_4DSBDC = 2,5-disulfhydrylbenzene-1,4-dicarboxylicacid), $M_2Cl_2(BTDD)(DMF)_2$ (M = Mn^{2+}, Fe^{2+}, Co^{2+}, Ni^{2+}; H_2BTDD = bis(1H-1,2,3-triazolo[4,5-b],[4,'5'-i]dibenzo[1,4]dioxin), and M(1,2,3-triazolate)$_2$ (M = Mg^{2+}, Mn^{2+}, Fe^{2+}, Co^{2+}, Cu^{2+}, Zn^{2+}, Cd^{2+}) (Figure 4) [17].

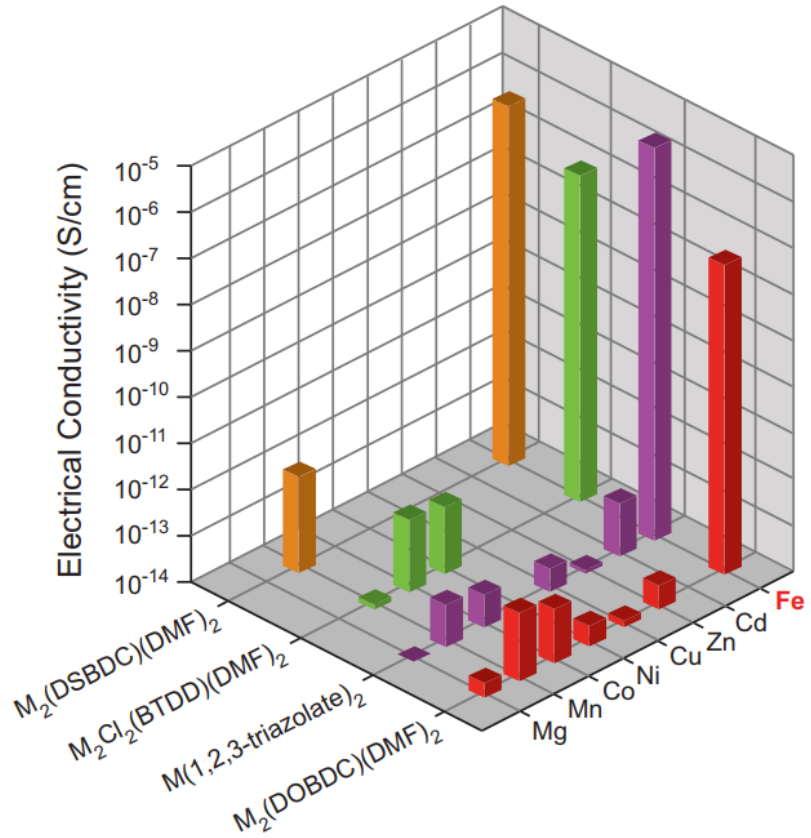

Figure 4 - Electrical conductivity in M2(DOBDC)(DMF)2, M2(DSBDC)(DMF)2, M2Cl2(BTDD)(DMF)2, and M(1,2,3-triazolate)2 measured at 300 K, in N2 atmosphere, and in the dark [17].

2.3.1 Zeolitic Imidazolate Frameworks

ZIF is a sub-family of MOFs formed from coordination of metal ions and imidazole derivatives. The metal-imidazole-metal bond forms an angle of 145°, the same angle as the silicon-oxygen-silicon bond in zeolites [18].

Commercially available ZIF-8 ($Zn(MeIm)_2$) is synthesized from zinc and 2-methyl-imidazole, and it is used as a core for core-shell materials and as a N-containing carbon precursor [19] [20]. ZIF-8 crystals derived carbon has a high nitrogen content and high surface area, but its conductivity is limited due to its amorphous nature. In contrast pyrolysis of ZIF-67 ($Co(MeIm)_2$) will have a graphitic structure with sacrificed nitrogen content [20]. Synthesis of ZIF-8 has been reported in both solvothermal processes or in aqueous systems [21].

2.3.2 Metal 1,2,4-Triazolate Frameworks

Having three N-donors 1,2,4-triazolates can behave like imidazolates to form similar structural units or isostructural 3D units. [22]

Metal triazolates have gained interest due to their spin crossover behavior and due to short metal-metal distances in framework which should result in a high charge hopping probability [23].

3 Materials and Methods

Description of the materials, including chemicals used and all the experimental procedures performed.

3.1 Synthesis of electrode materials

All the reagents used in this study were of laboratory grade and were used as received without any further purification (Table 1). Deionized water was purified by reverse-osmosis system (Purelab Maxima/ELGA), with a resistivity of 18.2 MΩ.cm at 25 °C. Solvents used in purification were of industrial grade purity.

Table 1 – Chemical reagents used in study

Chemical Reagent	Formula	Purity	Company
Zinc nitrate hexahydrate	$Zn(NO_3)_2 \cdot 6H2O$	99 %	Alfa Aesar
Iron (II) chloride tetrahydrate	FeCl2·4H2O	-	Nacalai Tesque
Iron (II) Sulphate Heptahydrate	FeSO4·7H2O	98 %	Nacalai Tesque
2-Methylimidazole	C4H6N2	99 %	Sigma-Aldrich
1,2,4-Triazole	C2H3N3	98 %	Sigma-Aldrich
Anhydrous methanol	CH3OH	-	ALPS Chem
Titanium foil, thickness: 0.05 mm	Ti	99.95 %	GoodFellow
N-methylpyrrolidone (NMP)	C5HNO	-	Mallinckrodt
Polyvinylidene difluoride (PVDF)	-(C2H2F2)n-	-	Aldrich
Super P (conductive carbon black)			TIMCAL

3.1.1 Synthesis of ZIF-8

This material was synthesized in an aqueous system. 2.32 g of Zn(NO3)2·6H2O was diluted in 16 g of deionized water and 22.70 g of 2-Methylimidazole (MeIm) was dissolved in 80 g of deionized water, solutions were then stirred for 24 hours at room temperature. The proportion of Zn2+ to MeIm was 1:35. Synthesis was adapted from Pan *et. al.* (2011) [21].

The precipitate formed was washed five times with methanol via centrifugation. It was then dried overnight at 80 °C.

3.1.2 Synthesis of Fe-MeIm-ST1

A solvothermal method is used in this synthesis. 1.08 g of $FeCl_2 \cdot 4H_2O$ was dissolved in 80 ml of methanol and 1.05 g of MeIm in another 80 ml of methanol. The solutions were then mixed with mechanical stirring for 10 minutes before transferring into a 200 ml sized autoclave. The autoclave was placed in a furnace at 95 °C for 16 hours. This procedure was adapted from the synthesis of ZIF-8 in Tang et al. [20].

The precipitate formed was washed five times with methanol via centrifugation and dried overnight at 80 °C.

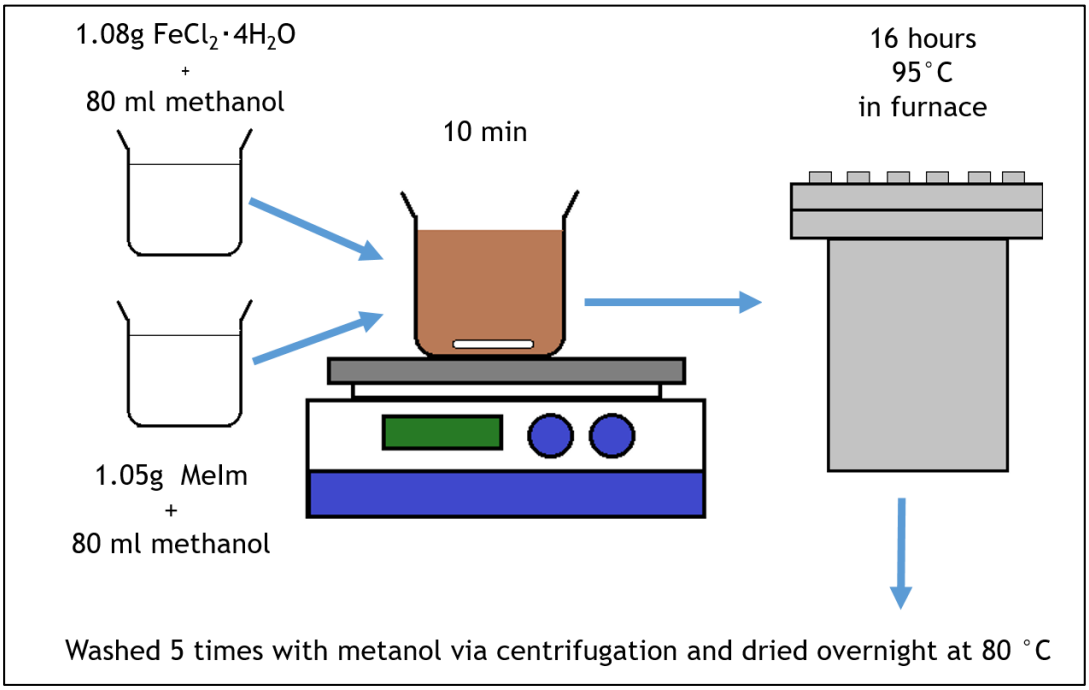

Figure 5 – Synthesis Diagram for Fe-MeIm-ST1

3.1.3 Synthesis of Fe-MeIm-ST2

The same procedure was used as Fe-MeIm-ST1 in chapter 3.1.2 with the exception of using 1.52 g of $FeCl_2 \cdot 4H_2O$ substituting Iron Chloride and using 2.26 g of MeIm. The proportion of Fe^{2+} to MeIm was 1:5.

3.1.4 Synthesis of Fe-Trz-ST

This material was also synthesized by a solvothermal method. 1.19 g of $FeCl_2 \cdot 4H_2O$ was dissolved in 80 ml of methanol and 414 mg of 1,2,4-Triazole (Trz) in 60 ml of methanol.

Proportion of Fe^{2+} to Trz was 1:1. The solutions were mixed together and stirred for 10 minutes and transferred into an autoclave.

The precipitate formed was washed five times with methanol via centrifugation and dried overnight at 80 °C.

3.1.5 Calcination

Materials were calcined in different conditions (table 2) either under vacuum or with nitrogen gas flow. Temperature of the furnace was raised at a rate of 1 °C/min and held at calcination temperature for 3 hours before returning to room temperature.

Table 2 – Conditions used for Calcination

	Material	Gas	Temperature (°C)
ZIF-8-C800	ZIF – 8	Nitrogen	800
Fe-Me Im-ST1-C800	Fe-MeIm-ST1	Nitrogen	800
Fe-MeIm-ST2-V300	Fe-MeIm-ST2	Vacuum	300
Fe-MeIm-ST2-V240	Fe-MeIm-ST2	Vacuum	240
Fe-MeTrz-ST1-V600	Fe-Trz-ST1	Vacuum	600
Fe-MeTrz-ST1-V300	Fe-Trz-ST1	Vacuum	240

3.2 Analysis and Characterization

3.2.1 Phase Identification

Phase Identification is carried out by X-ray diffraction (XRD) analysis, which is used to determine constituents and crystalline phases. The XRD was performed on the diffractometer (X'pert/Philips) with Cu Kα radiation (λ = 1.418 Å). The X-Ray generator equipped with a graphite monochromator was operated at 40 kV and 40 mA. The width angle of solar and divergent slits is 1.0 °. In addition, the reflection data of powder samples was mostly collected under a continuous¬scanned θ - 2θ mode at a scan-rate of 4 °/min. The scan range is in the range of 5 ° - 80 °.

3.2.2 Microstructure Characterizations

Surface morphology of the particle samples and films was on a field-emission scanning electron microscope (FEI Nova NanoSEM 230 and LEO 1530). The powder samples were dispersed in a methanol solution under sonification and deposited on a copper foil which was then dried on a hotplate. The samples were dried overnight with vacuum. Before examination, the samples

were coated with gold by ion sputter. The accelerated voltage of electron gun was 5 and 20 kV, respectively. The signals detected secondary electrons and back-scattered electrons.

Transmission electron microscopy (TEM) analysis was carried out using an electron microscope (H7100/Hitachi) operated at 100 kV. The particles were ultrasonically dispersed in methanol and a drop of dilute solution was placed on a carbon supported copper grid.

3.3 Electrochemical Characterization

3.3.1 Preparation of Electrodes

The Titanium-based electrodes were prepared via solvent-casting method. First, the active material was grinded with Super P, a conductive carbon black using a mortar and pestle. Once the ground powders were homogeneous, a binder (Polyvinylidene fluoride) in a N-methylpyrrolidone (NMP) solvent was added to the ground powder. After stirring for 10 minutes the slurry is cast on a Titanium strip and spread. The electrodes were heated at 110 °C for 6 hours under vacuum to remove the solvent. After heating, the electrodes were cut into 1 cm width pieces, with the active material covering 1 cm^2 of the strip.

Table 3 – Recipe for working electrodes

Material	Weight Percentage (%)
Active Material	80
Super P	10
PVDF	10

3.3.2 Cyclic Voltammetry

This convenient and sensitive method is used to distinguish electrochemical characteristics of device. An Ideal EDLC's voltammogram shows a rectangular shaped profile. For a pseudocapacitor, superficial faradaic reactions happen during the charging or discharging and some redox peaks appear in the voltammogram. In a real situation the profile is affected by the resistance of the electrolyte and the contact resistance between the active material and the current collector, this delays the response, which leads to a slant of the cyclic voltammogram (CV).

The CV was conducted on an electrochemical analyzer (CHI 405 A Instrument). The cells of different active materials were characterized on a three-electrode system which is shown in Figure 6 consisting of a platinum counter electrode, an Ag/AgCl reference electrode and the working electrode.

The data of the voltammogram is modified from a Current vs. Potential to display specific capacitance vs. Potential, this is done by applying eq. (3).

$$C = \frac{I}{s \times w} \quad (3)$$

Where I was the current measured with the potentiostat, s is the potential scan rate and w, the mass of the active material. The specific capacitance is then calculated from half of the area between the charge and discharge curves divided by the voltage window.

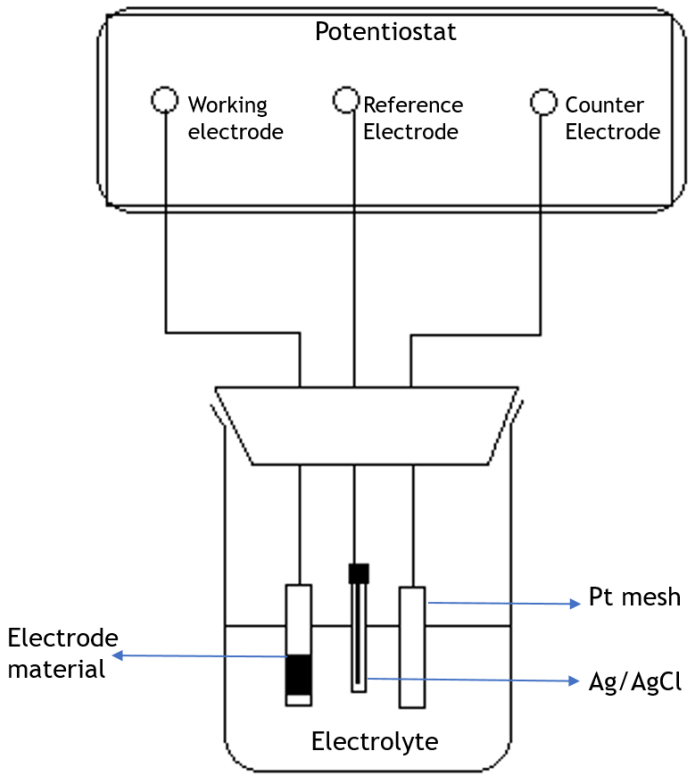

Figure 6 – Configuration of the three electrode cell.

3.3.3 Chronopotentiometry/Galvanostatic Charge and Discharge

Complementing cyclic voltammetry, chronopotentiometry provides a different way to examine electrochemical performance. It monitors potential as function of time under a

constant charge and discharge current. The setup was the same as the three electrode used in CV measurement (Figure 6).

3.4 Surface Area and Pore Structure Analysis

The BET (Brunauer, Emmet and Teller) surface area and pore-size distribution of the materials was determined by nitrogen adsorption with a surface area analyzer (ASAP-2010/Micrometrics). BET method involves multi-layer adsorption of which the equation is described as:

$$\frac{P}{V(P_0-P)} = \frac{1}{V_m c} + \frac{(c-1)}{V_m C}\frac{P}{P_0} \qquad (4)$$

Where V is the volume of adsorbed nitrogen (cm^3/g), P is the pressure of adsorbed gas, P_0 is the saturated vapor pressure, V_m is the volume of mono-layer adsorbed nitrogen and c is the BET constant. The linear relation of $P/V(P_0-P))$ and P/P_0 can be obtained, which gives a slope of $(c-1)/V_m c$ and from this, the specific surface area can be calculated based on the volume of adsorbed nitrogen [22]. BJH (Brunauere, Joyner and Halender) scheme for determination of mesopore distribution is based on the Kelvin equation and thickness equation, showing the relation between relative pressure and pore size. 8-points measurement was utilized for determining BET surface area, in which the relative pressure ranging from 0.06 and 0.2. 55 points were measured for the characterizing mesopores. The interval time was set at 20 seconds.

3.5 Thermal Analysis

3.5.1 Thermogravimetric analysis

Thermogravimetric analysis (TGA) was performed using a PerkinElmer Diamond TGA-DTA thermal analyser. TGA can monitor the mass of samples while heated at a constant rate. The heating of the sample can be performed with different gases and for these tests nitrogen gas was used.

TGA thermal curves will display the mass percentage of the sample vs. temperature.

4 Results and discussion

In this chapter each material is characterized one by one, first by presenting the results of characterization tests followed by electrochemical tests.

4.1 Characterization of ZIF-8

The XRD pattern of the synthesized ZIF-8 in this study is shown in Figure 7. The XRD pattern matches with the simulated structure found in Park *et. al.* (2006). These correspond to a sodalite zeolite-type topology. [23]

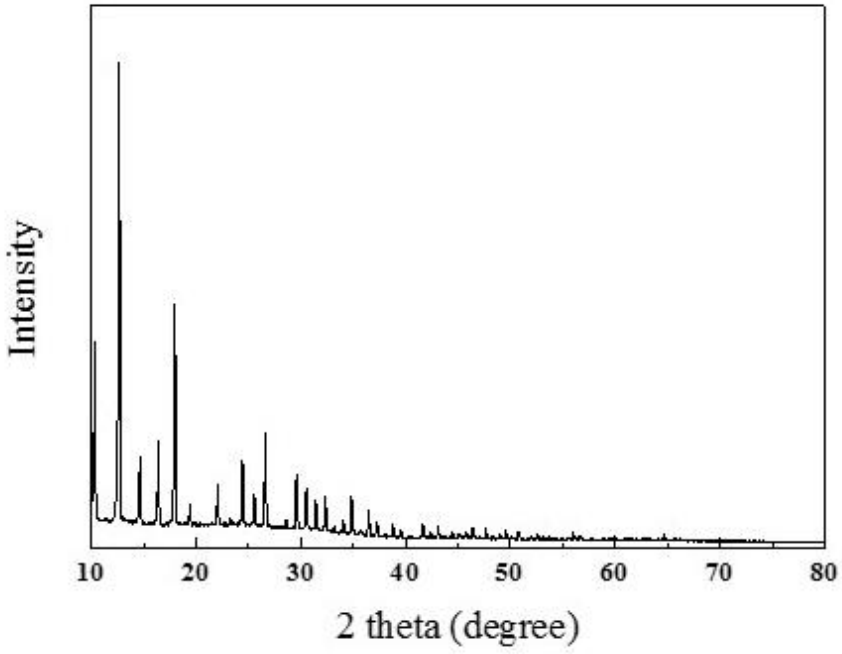

Figure 7 – XRD pattern for ZIF-8.

Morphology of the material is presented in Figure 8 from SEM images. The material does not show the typical ZIF-8 cubic or rhombic shape, rather it shows interlinked particles.

The material was subjected to calcination in nitrogen gas at 800 °C. this process transforms the ZIF-8 into a nitrogen-doped carbon [20] ZIF-8-C800. The XRD of ZIF-8-C800 shows an amorphous structure (Figure 9).

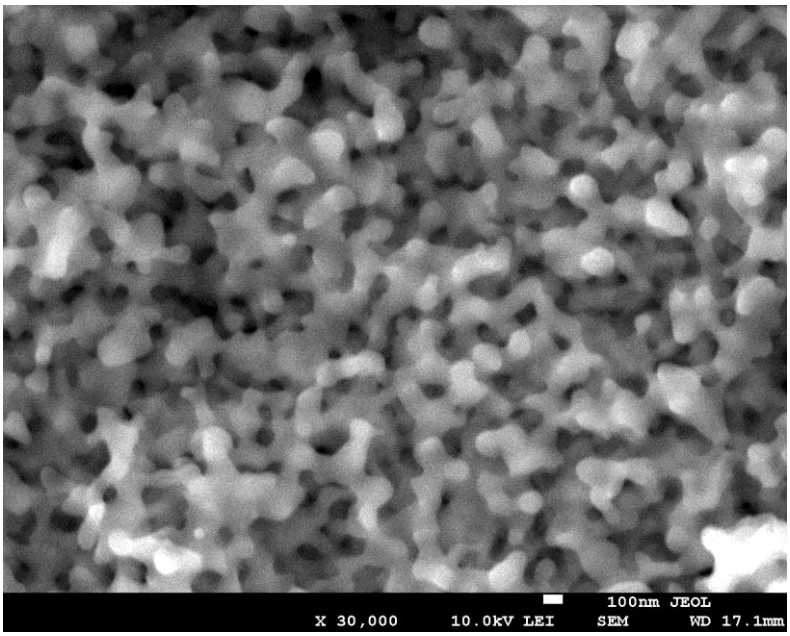

Figure 8 – SEM image ZIF-8.

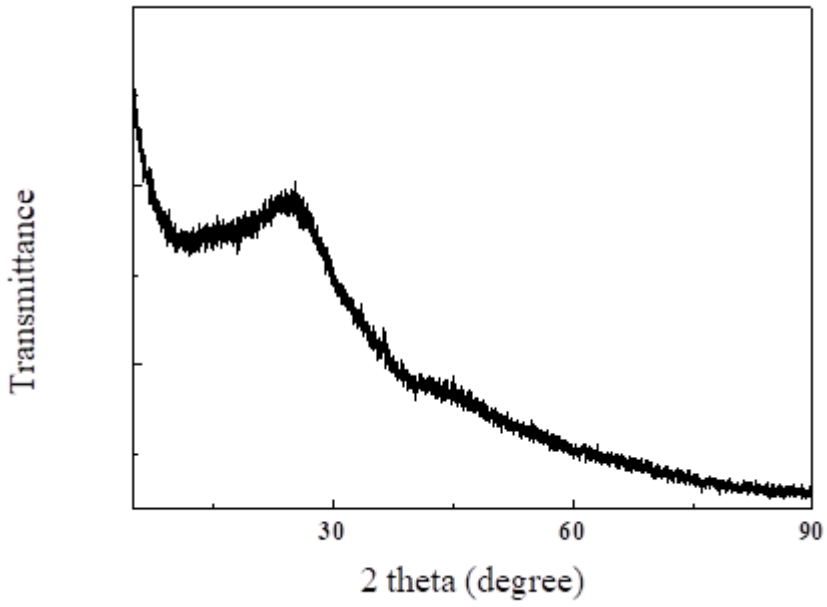

Figure 9 – XRD of ZIF-8-C800.

4.1.1 Electrochemical Characterization of ZIF-8-C800

The ZIF-8-C800 electrode was made using the method described in Chapter 3.3.1. The electrode was tested in a 1.0 M Li_2SO_4 electrolyte. The voltage window was found by gradually increasing it, tested with cyclic voltammetry at a scan rate of 20 mV/s. The voltage window selected for further tests was of 1.7 V, from -0.9 V to 0.8 V (Figure 10). Cycling of this electrode

forms the shape of a typical EDLC. After 30 cycles the shape had stabilized and had a specific capacitance of 156 F/g (Figure 11). Increasing the scan rate decreased the specific capacity drastically, which may occur because ions did not have sufficient time to penetrate the pores of the material, thus accumulating only on the outer surface (Figure 12) (Figure 13). These results demonstrate that using lithium sulphate as an electrolyte for a ZIF-8 derived N-containing carbon electrode has a high working voltage. Charge and discharge tests (Figure 14) of this electrode shows an almost symmetrical charging and discharging, this is the common result for EDLCs. A pseudocapacitor would have irregularities in the curves.

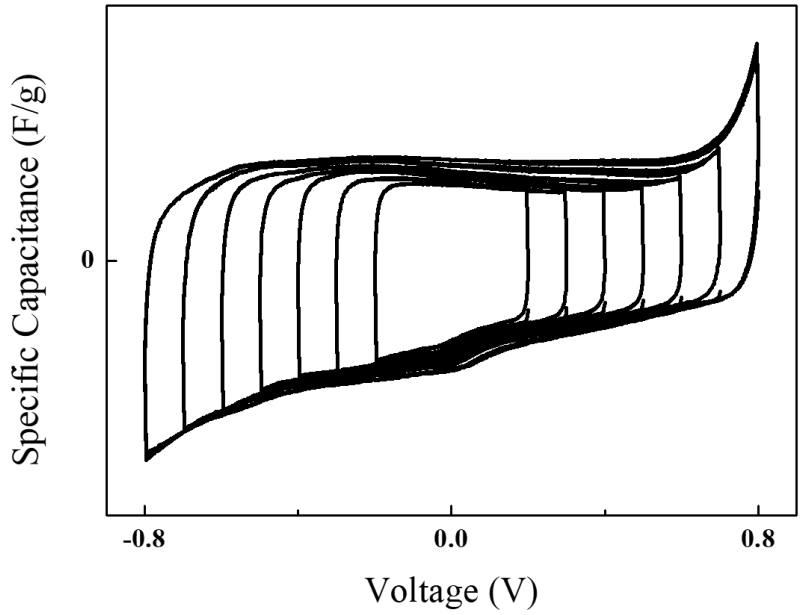

Figure 10 – CV of ZIF-8-C800 in 1.0 M Li_2SO_4 with different voltage windows.

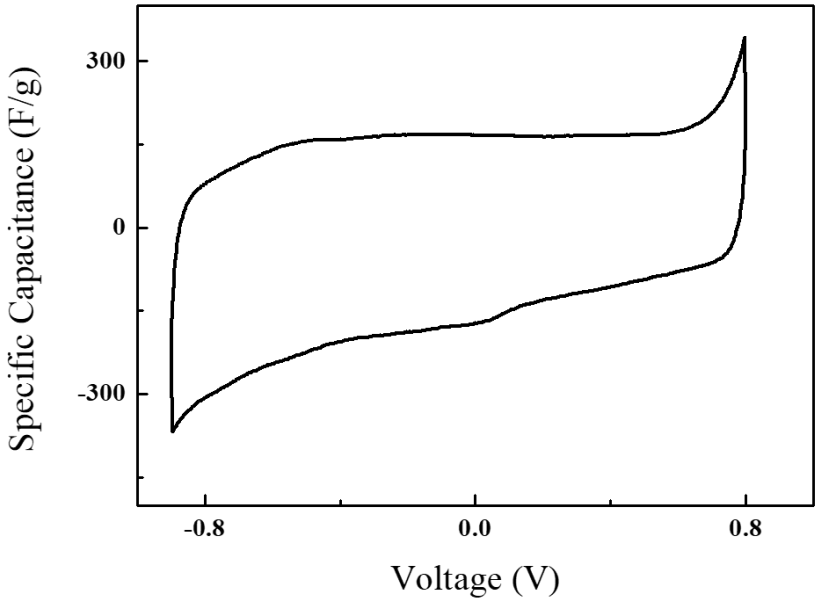

Figure 11 – CV of ZIF-8-C800 in 1.0 M Li_2SO_4 after 30 cycles.

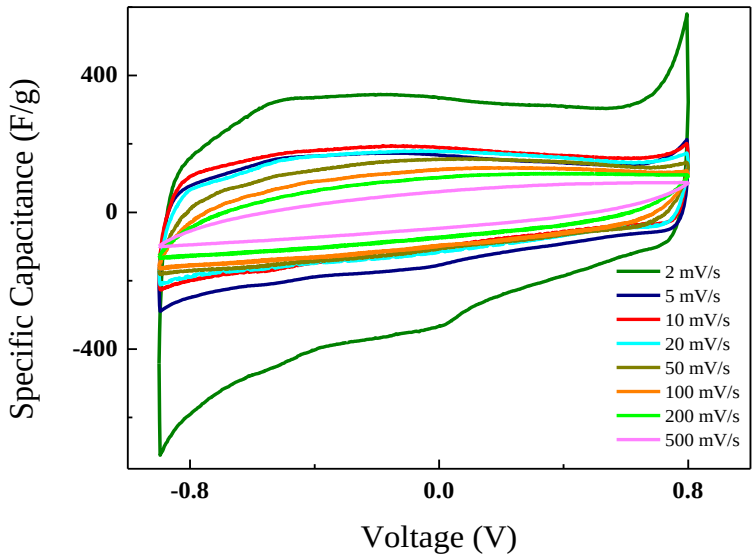

Figure 12 - CV of ZIF-8-C800 in 1.0 M Li_2SO_4 with different scan rates.

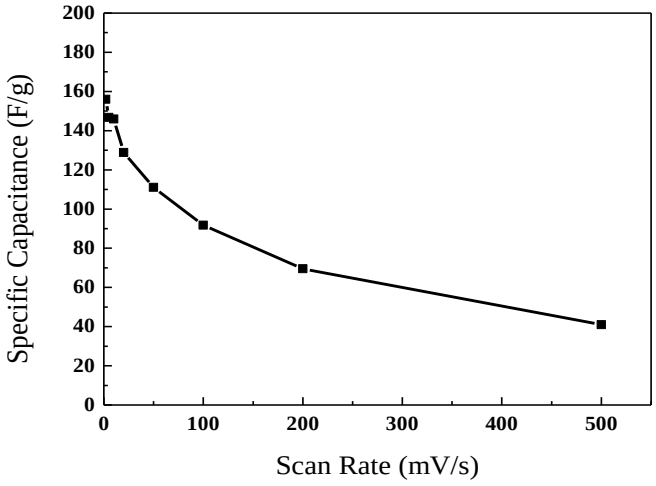

Figure 13 – Specific capacitances of ZIF-8-C800 in 1.0 M Li_2SO_4 at different scan rates.

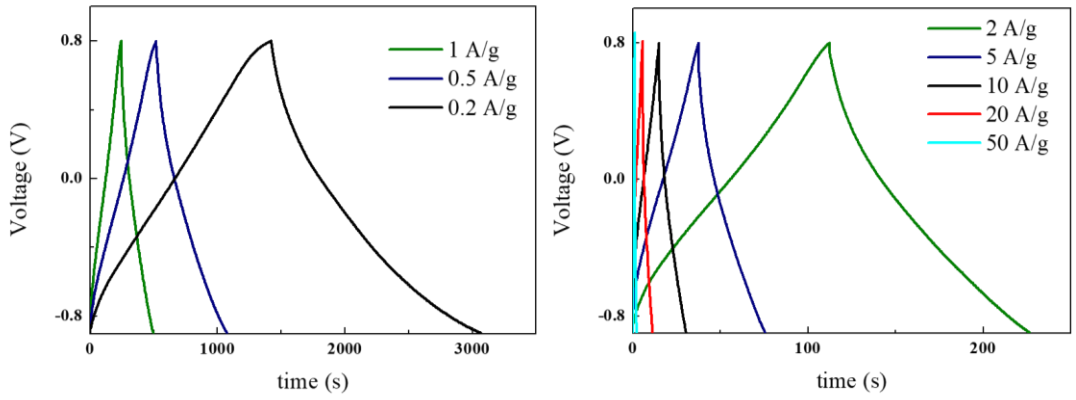

Figure 14 – Galvanostatic Charge and Discharge curves of ZIF-8-C800 in 1.0 M Li_2SO_4 with different current densities.

4.2 Characterization of Fe-MeIm-ST1

2-MethylImidazole (MeIm) was used as an organic ligand with an Fe^{2+} metal containing unit with the objective of obtaining a Fe^{2+} ZIF. Fe-MeIm-ST1 was the material obtained with the methods described in chapter 3.1.2.

XRD of Fe-MeIm-ST1 shows a crystalline pattern but doesn't match peaks from the X'Pert HighScore database (Figure 15). The SEM images in Figure 16 demonstrates an agglomeration of particles with fine particles on the surface.

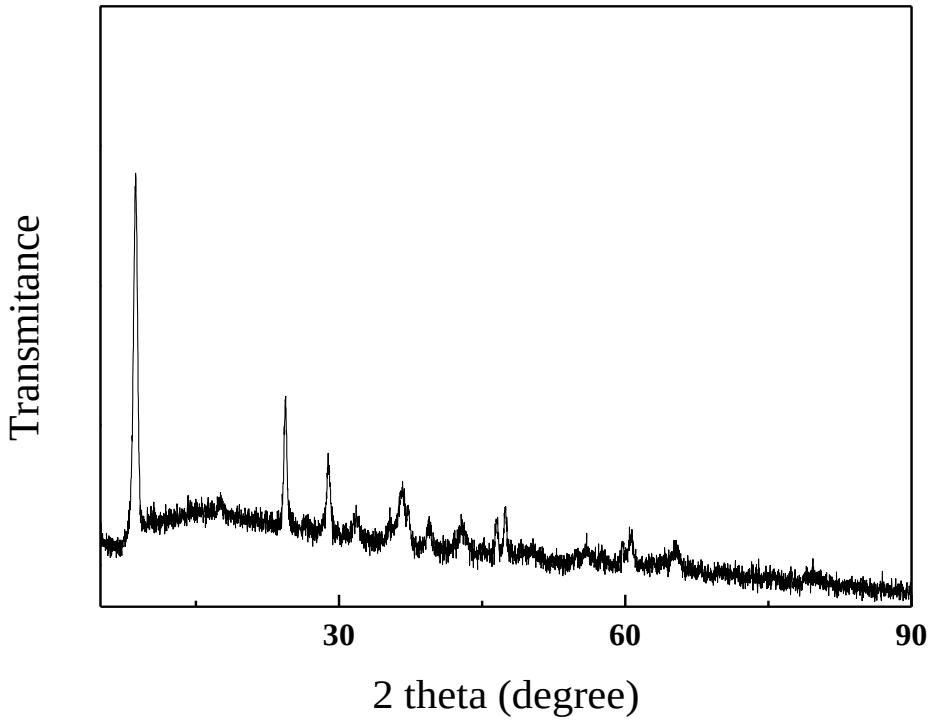

Figure 15 –XRD pattern of Fe-MeIm-ST1.

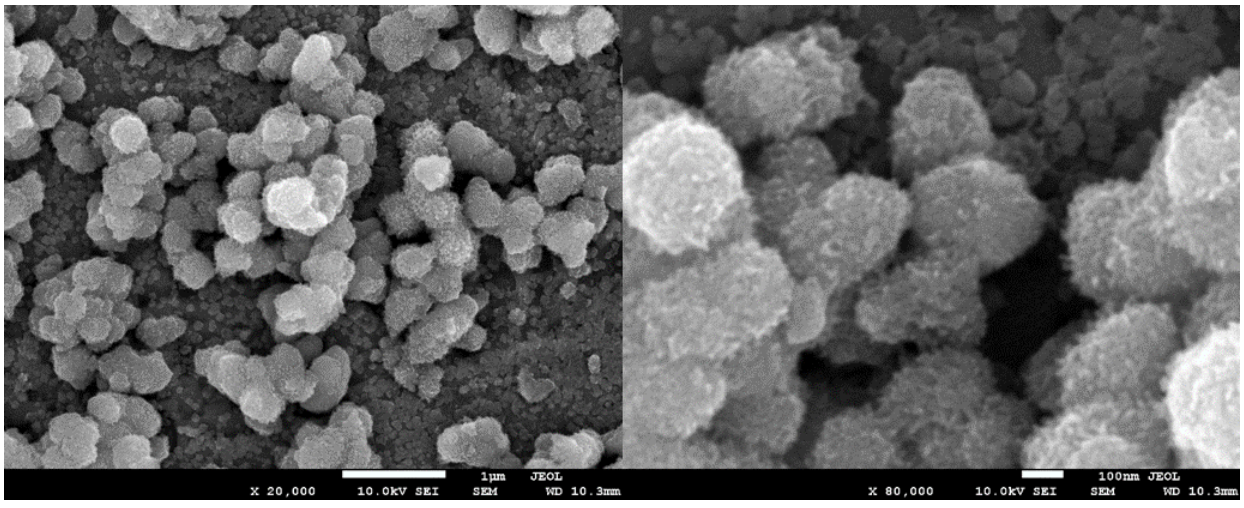

Figure 16 – SEM images of Fe-MeIm-ST1, on the left at ×20,000 and on the right ×80,000 magnification.

The adsorption and desorption curves have an H2 type hysteresis which have bottleneck pores (Figure 17). Total BET surface area is 130 m^2/g, also determined by nitrogen adsorption. Figure 18, a Barrett-Joyner-Halenda pore volume distribution plot of Fe-MeIm-ST1 shows a peak of pores at approximately 6 nm from.

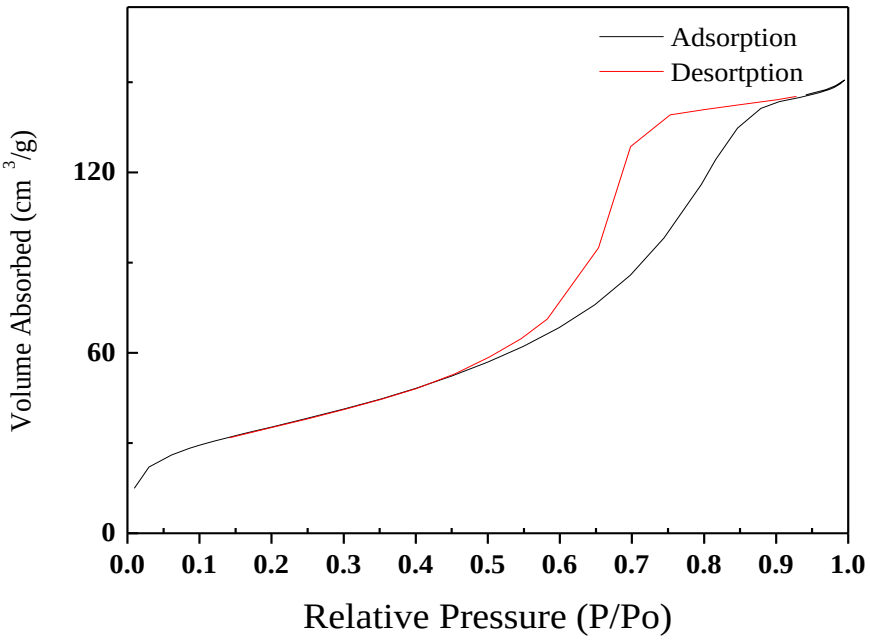

Figure 17 – Nitrogen adsorption and desorption isotherm for Fe-MeIm-ST1.

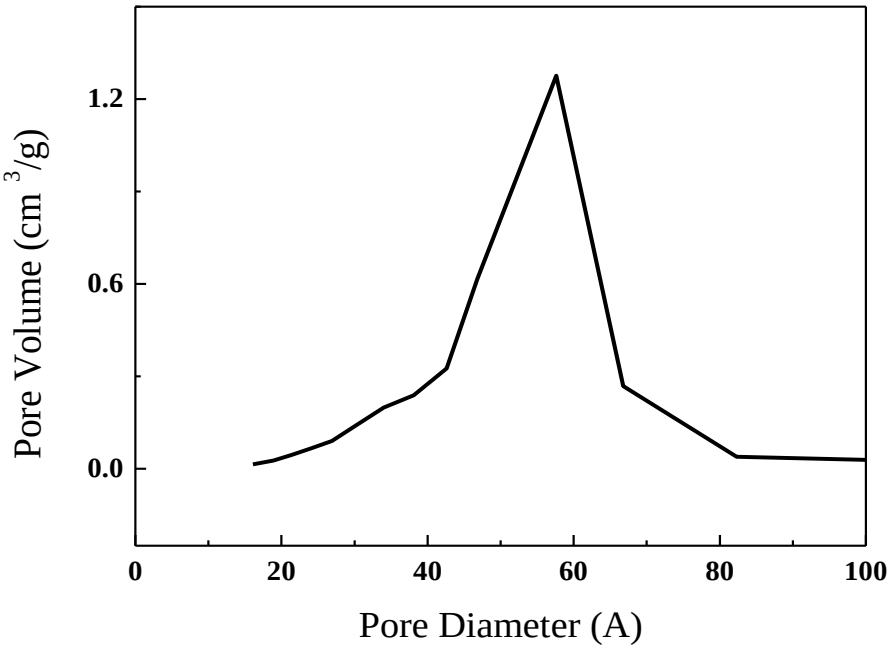

Figure 18 – Barrett-Joyner-Halenda pore distribution plot Pore volume distribution of Fe-MeIm-ST1.

After Calcination at 800 °C, Fe-MeIm-ST1-C800 forms an oxide material with some amorphous content. This is deduced through the XRD pattern (Figure 19). The pattern shows

the same peaks as Magnetite (Fe_3O_4) [24]. The BET surface area Fe-MeIm-ST1-C800 is 7.5 m^2/g (Figure 21). Loss in surface area is related to the collapse of the pores at higher temperature during calcination. Fe-MeIm-ST1-C800 SEM images show particles of a tetragonal crystal shape (Figure 20).

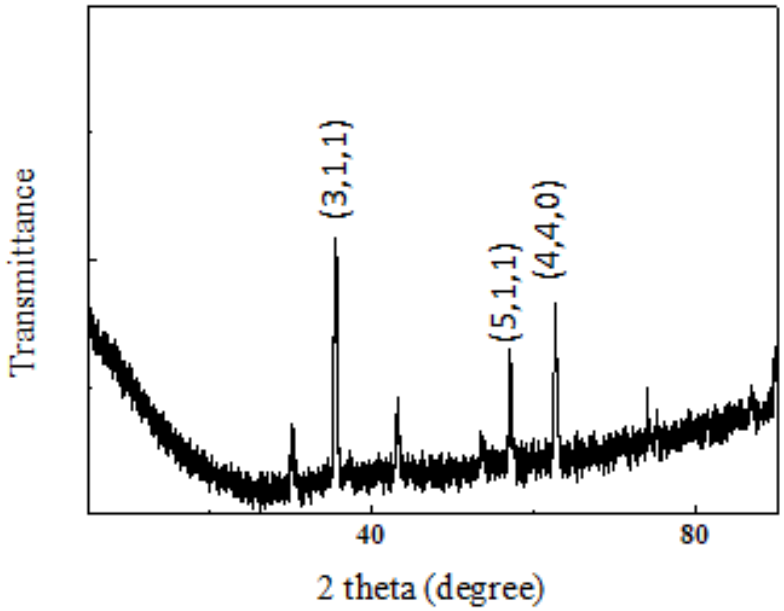

Figure 19 - XRD pattern of Fe-MeIm-ST1-C800

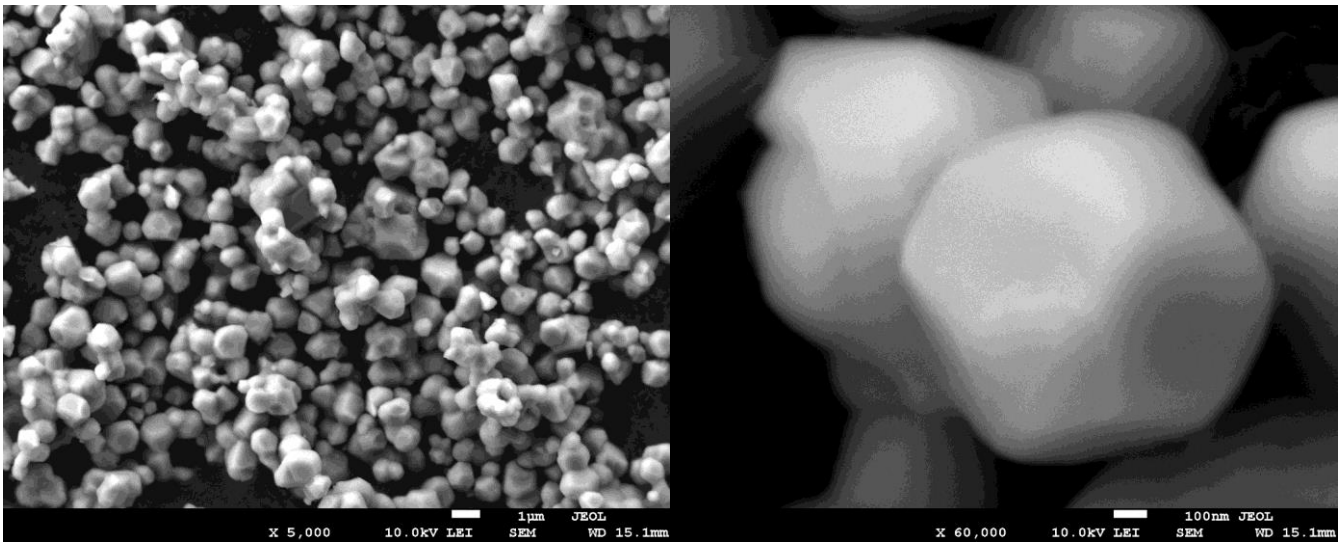

Figure 20- SEM images of Fe-MeIm-ST1, on the left at ×5,000 and on the right ×40,000 magnification

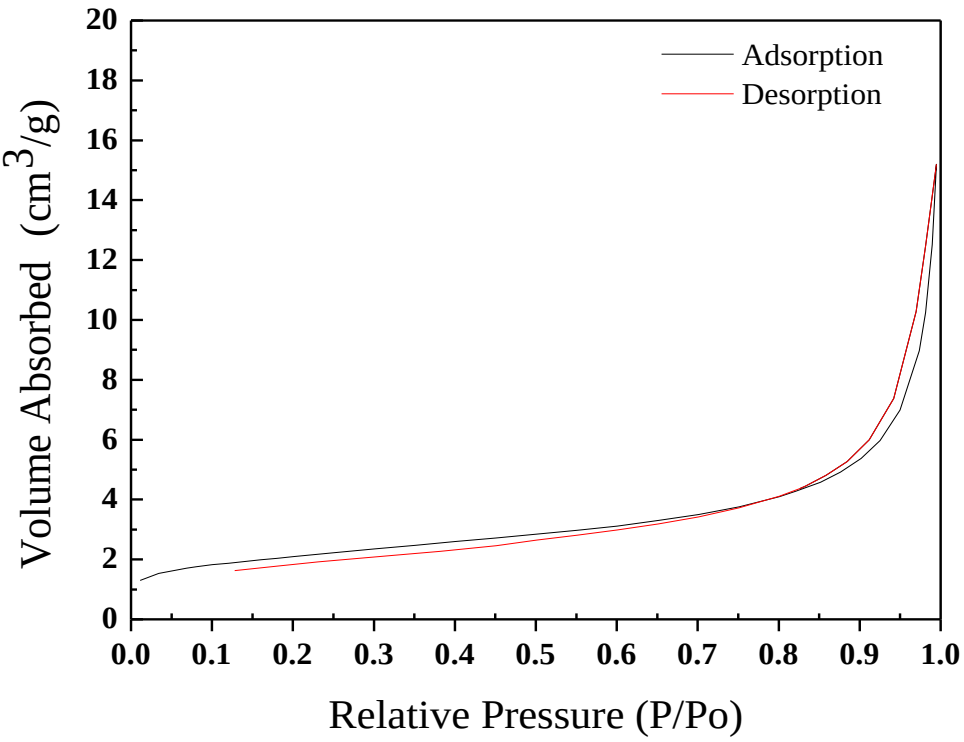

Figure 21 – Nitrogen adsorption and desorption isotherm for Fe-MeIm-ST1-C800

A TGA of Fe-MeIm-ST1 was performed to determine a temperature for calcination which would preserve the porous structure of the material. The results are displayed on Figure 22 and show that there is a significant loss in weight percentage after 240 °C.

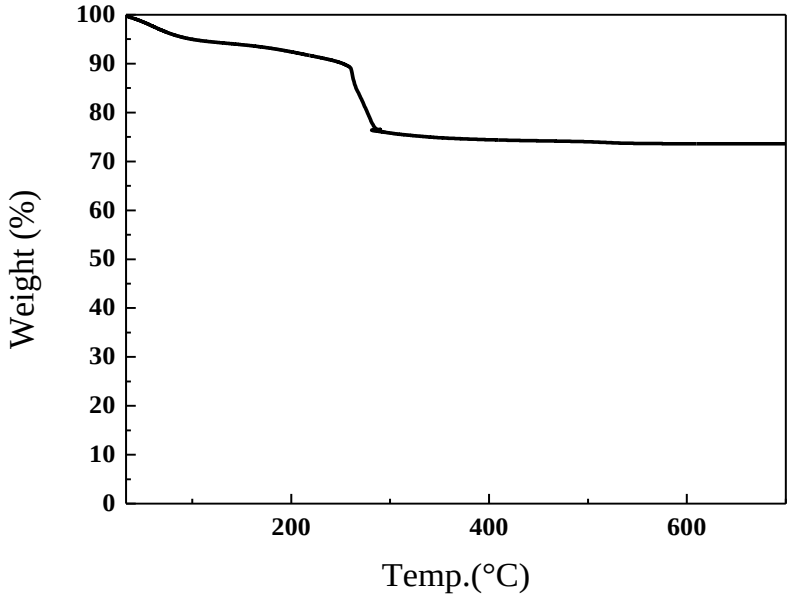

Figure 22 – TGA of Fe-MeIm-ST1

4.2.1 Electrochemical Characterization of Fe-MeIm-ST1-C800

This material was tested with 1.0 M Li_2SO_4 electrolyte. Cyclic Voltammetry was used to find the voltage window. At voltages lower than -0.1 V, the material had redox reactions and above this voltage it acted like an EDLC with low capacitance (Figure 23).

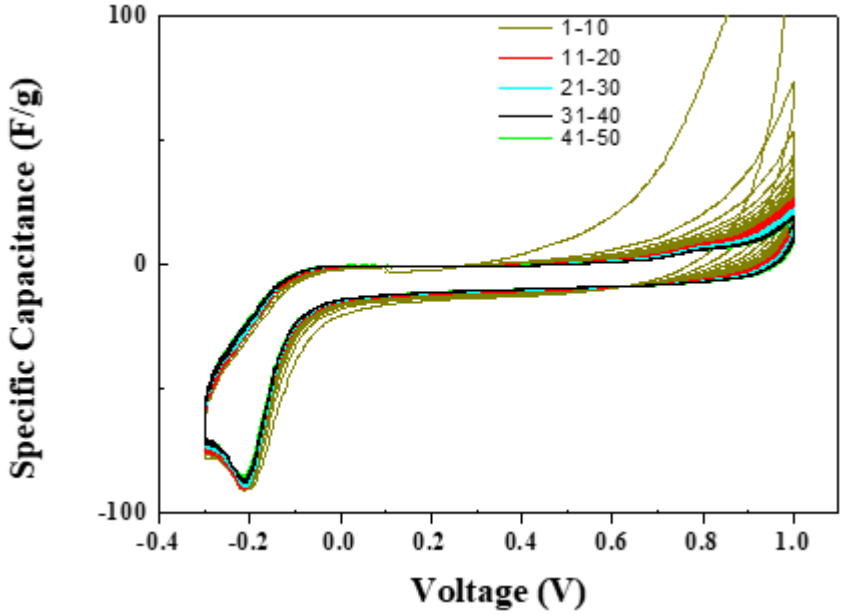

Figure 23 – CV of Fe-MeIm-ST1-C800 with Li_2SO_4 of first 50 cycles

4.3 Characterization of Fe-MeIm-ST2

Although not as pronounced as in Fe-MeIm-ST1, the XRD pattern for Fe-MeIm-ST2 (Figure 24) presents the same peaks as those seen for the previous material (Figure 15). The SEM images in Figure 25 show that the material forms hollow particles which could increase the amount of surface area accessible to the electrolyte. Through EDX we know that the material on the surface has a composition on the surface of 56% carbon, 32% oxygen and 12% iron in atomic percentage. TEM images in Figure 26 show that that the material is made from smaller rod-like particles which have aggregated. TGA was not performed on this material, but since the material presented a similar XRD pattern to Fe-MeIm-ST1, it is hypothesized that the TGA curve of Fe-MeIm-ST2 would be similar to that of Fe-MeIm-ST1 (Figure 22). Fe-MeIm-ST2 was calcinated under vacuum at 240 °C and 300 °C without visible changes in structure, forming Fe-MeIm-ST2-V240 and Fe-MeIm-ST2-V300 respectively.

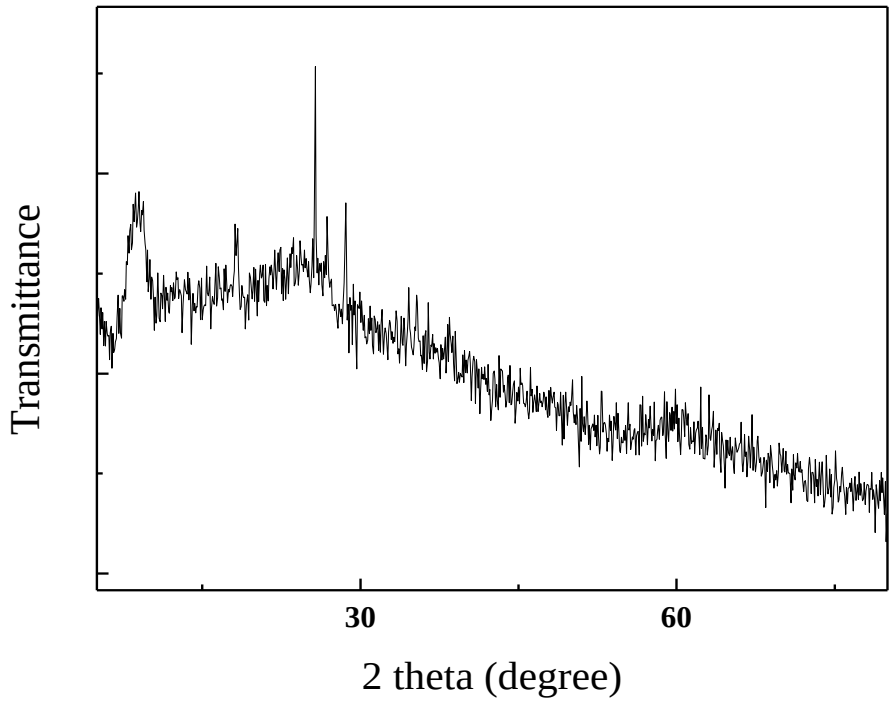

Figure 24 – XRD pattern of Fe-MeIm-ST2

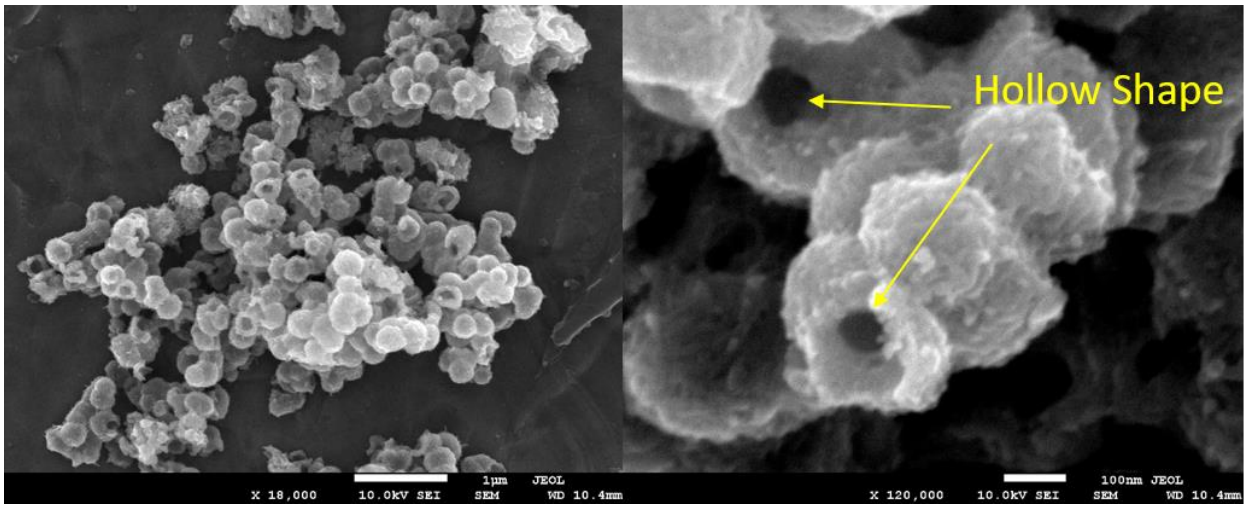

Figure 25 – SEM images of Fe-MeIm-ST2, on the left at ×18,000 and on the right ×120,000 magnification

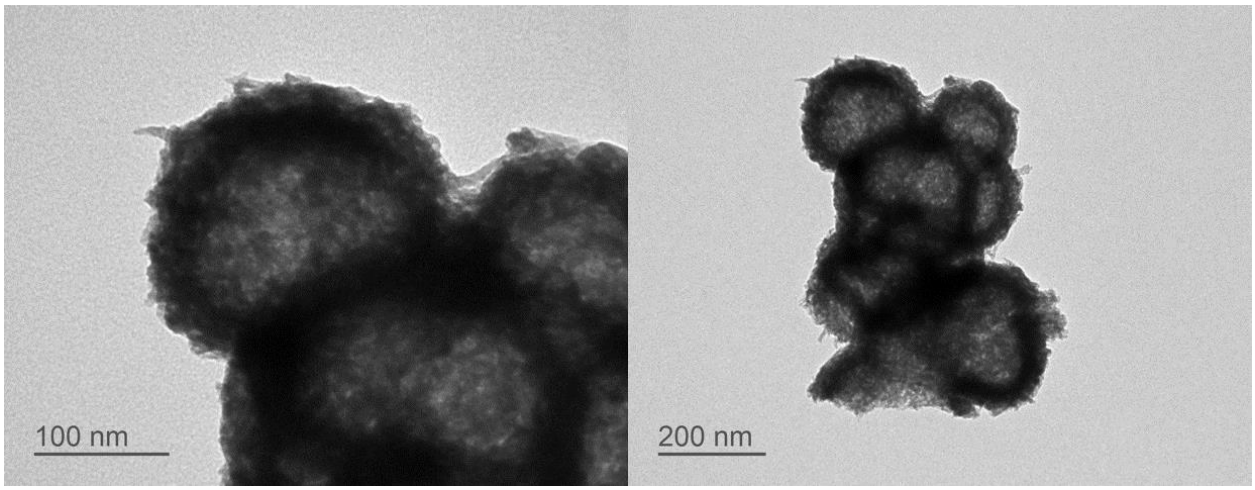

Figure 26- TEM images of Fe-MeIm-ST2.

4.3.1 Electrochemical Characterization of Fe-MeIm-ST2-V240

For this material the electrolyte used was sodium sulphite(Na_2SO_3). Na_2SO_3 has been tested with Fe_3O_4 electrodes with reversible redox reactions resulting in pseudocapacitance [25]. Pseudocapacitance results from SO^{3-}/S^{-2} redox couple as is presented in Figure 28 [26]. When tested with different voltage windows, it showed its highest capacitance from -1 to 0.1 V of 98 F/g (Figure 27). Testing Fe-MeIm-ST2-V240 with this electrolyte showed better performance than of Fe-MeIm-ST1-C800 with lithium sulphate, but the material did not show stability while cycling.

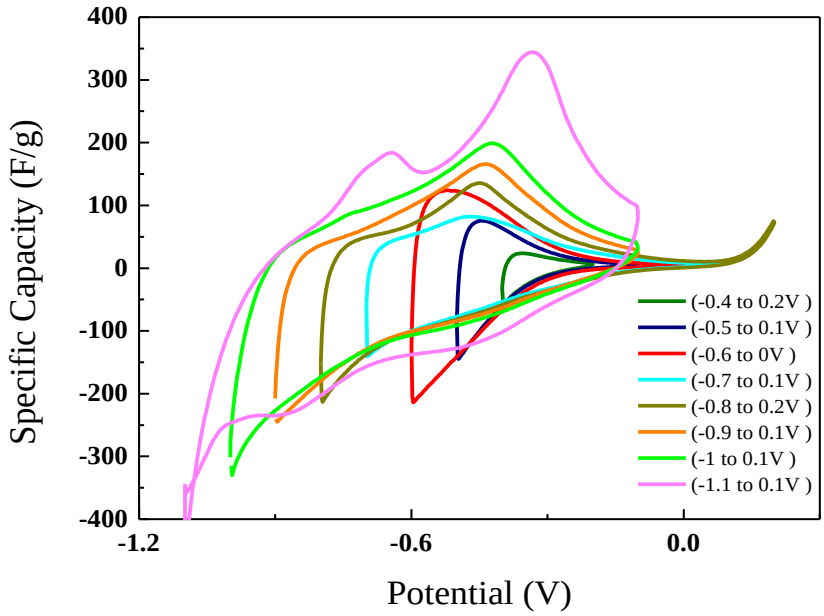

Figure 27 – CV of Fe-MeIm-ST2-V240 in 1.0 M Na_2SO_3 with different voltage windows.

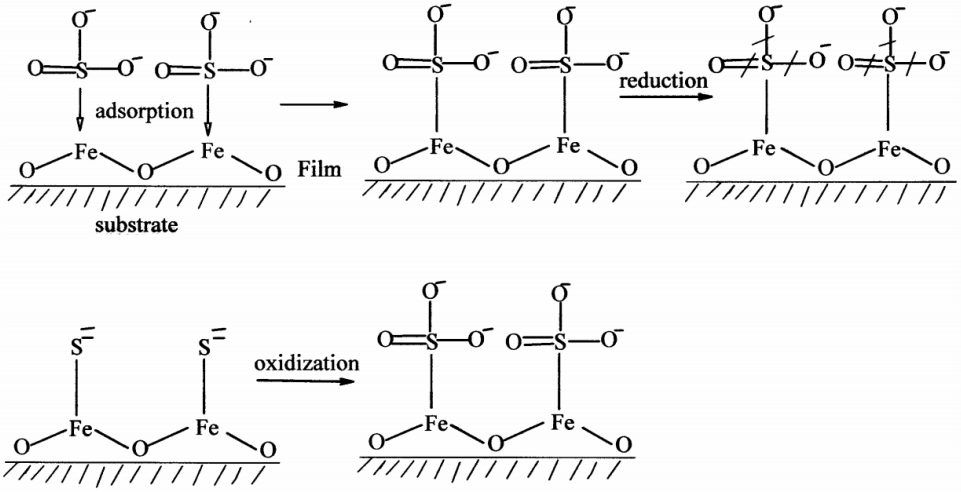

Figure 28 - Schematics of the proposed pseudocapacitance mechanism involving SO^{3-}/S^{-2} [26].

4.3.2 Electrochemical Characterization of Fe-MeIm-ST2-V300

This electrode was also tested with Na_2SO_3. The highest capacitance was achieved between -0.5 V and 0.5 V of 157 F/g (Figure 29). Scanning at higher scan rates decreased drastically the capacitance of the material (Figure 30). The lower specific capacitance achieved in Figure 30 compared to that in Figure 29 at 2 mV/s scan rate is due to the electrode not being changed between tests and the denaturing of the active material at higher voltage windows. Despite

this, of all the new materials tested, Fe-MeIm-ST2-V300 showed the best results, suggesting a potential application as an electrode material.

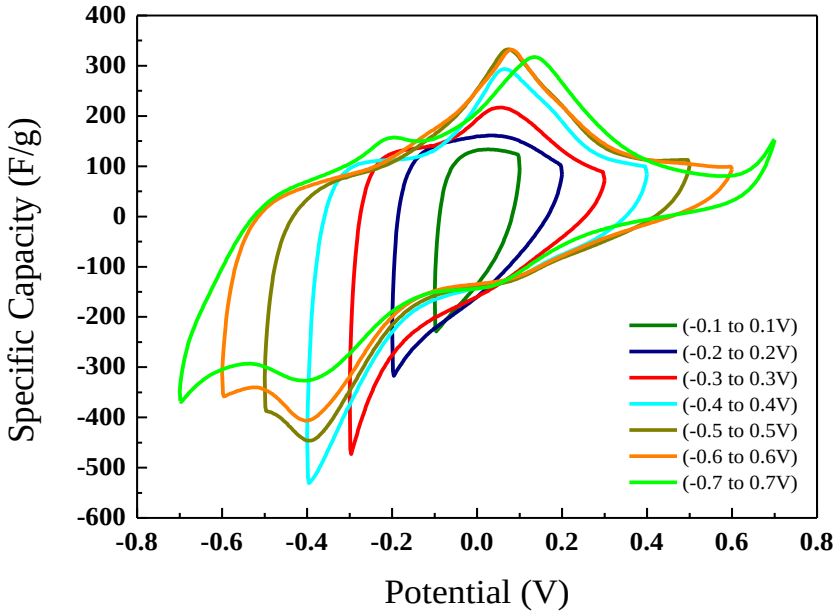

Figure 29 – CV of Fe-MeIm-ST2-V300 with 1.0 M Na_2SO_3 with different voltage windows.

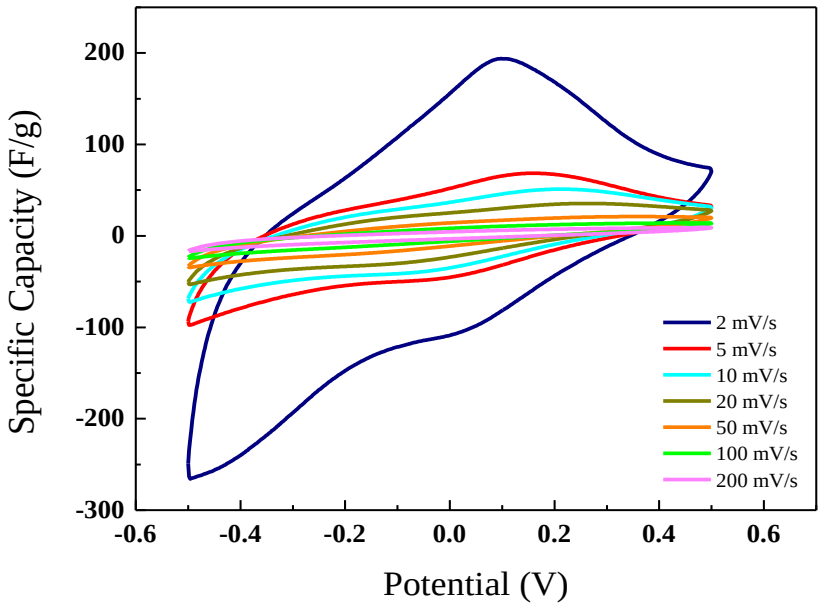

Figure 30 -CV of Fe-MeIm-ST2-V300 in 1.0 M Na_2SO_3 with different scan rates.

4.4 Characterization of Fe-Trz-ST1

XRD pattern of Fe-Trz-ST1 shows a crystalline pattern, but peaks do not match those in X'Pert HighScore software database (Figure 31). The material formed a rod morphology, in a three dimensional cluster radiating from a central point, like spokes of a wheel (Figure 32). EDX of the material showed of composition of 56 % of carbon, 9 % of nitrogen, 24 % of oxygen and 11 % of Iron in atomic percentage.

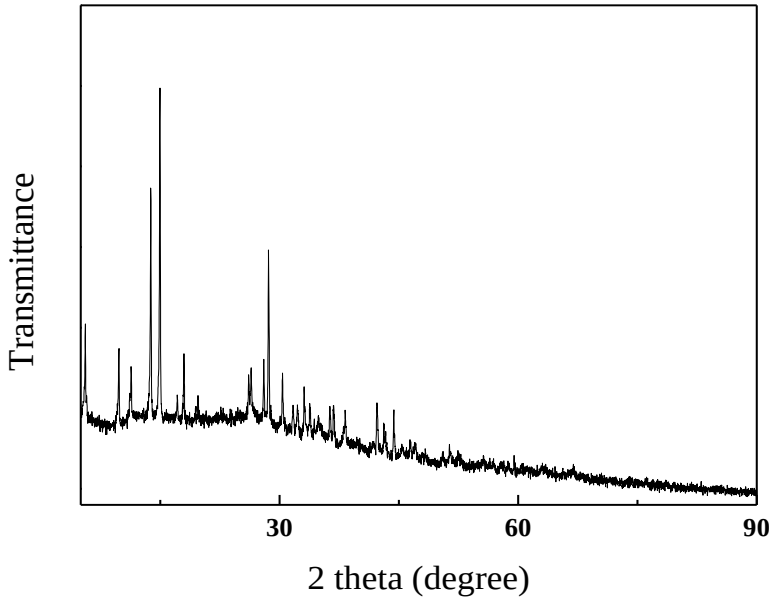

Figure 31 - XRD pattern of Fe-Trz-ST1

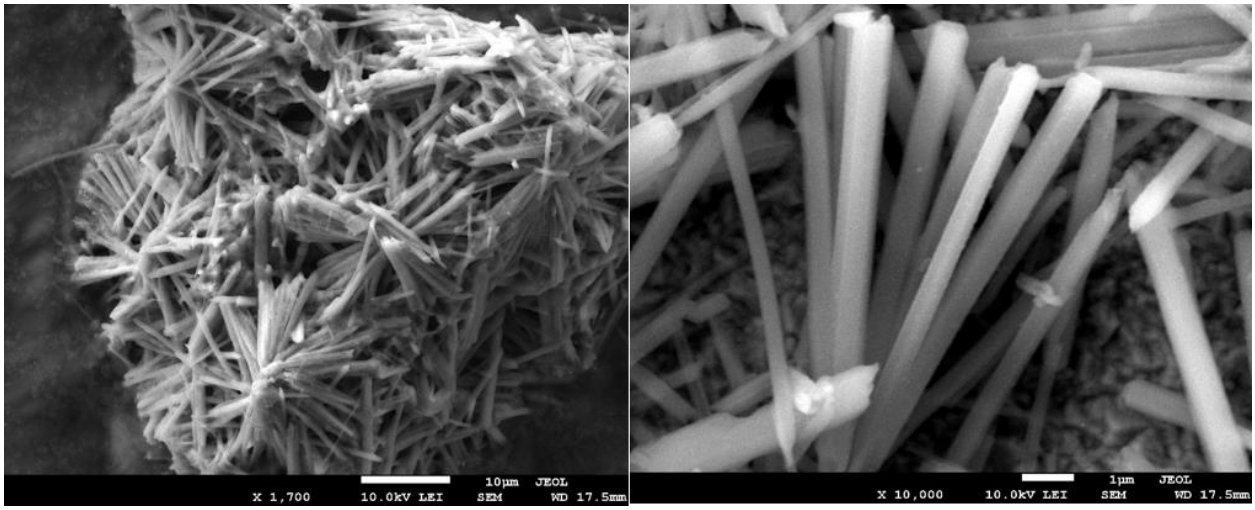

Figure 32 - SEM images of Fe-Trz-ST1, on the left at ×1,700 and on the right ×10,000 magnification

The BET surface area of Fe-Trz-ST1 was calculated as 564 m^2/g. and the nitrogen adsorption and desorption curves are those of a non-microporous material (Figure 33). The TGA performed under nitrogen gas is displayed on Figure 34. TGA shows that there is a significant loss of material when heated above 300 °C. Fe-Trz-ST1-V600 after calcination at 600 °C under vacuum, had a composition of 37% iron, 50% oxygen and 12% carbon, which was tested with EDX. From the TGA and composition of Fe-Trz-ST1-V600, we can see that most of the carbon and nitrogen content is lost around 300 °C. The change in composition also led to a change in structure, with the material forming an iron oxide of a tetragonal crystalline structure (Figure 35). When heated up to 240 °C under vacuum to form Fe-Trz-ST1-V240 the morphology of the material did not change.

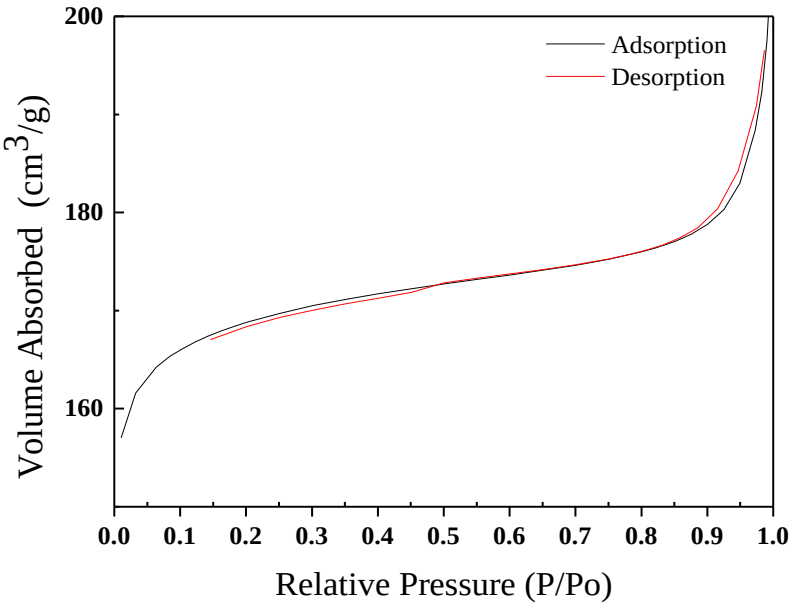

Figure 33 – Nitrogen adsorption and desorption isotherm for Fe-Trz-ST1

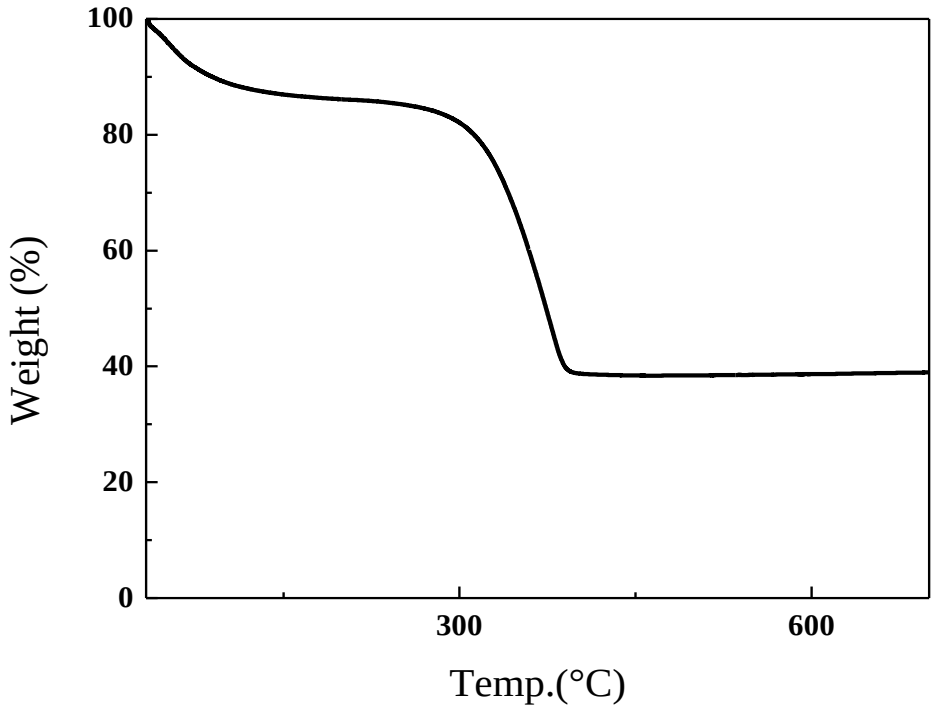

Figure 34 – TGA of Fe-Trz-ST1 under nitrogen gas

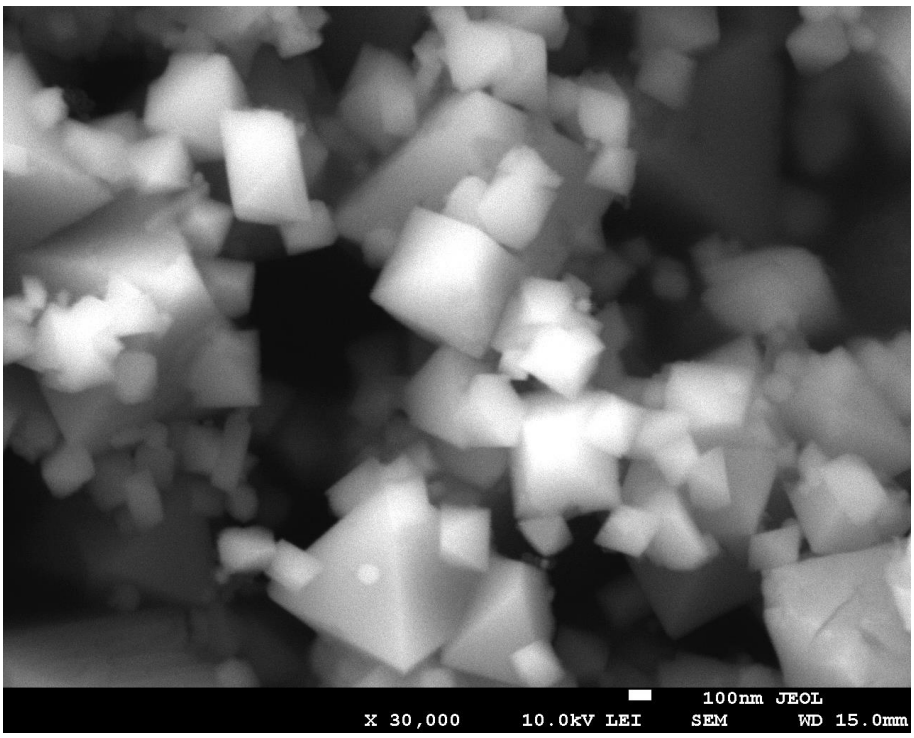

Figure 35 – SEM of Fe-Trz-ST1-V600 at x30,000 magnification

4.4.1 Electrochemical Characterization of Fe-Trz-ST1-V600

CV was first performed with Li_2SO_4 electrolyte. The electrode's voltage window of the electrode went from -1.1 to 0.5 V. However the cycling was not stable and rapidly decreased, as is depicted in Figure 29.

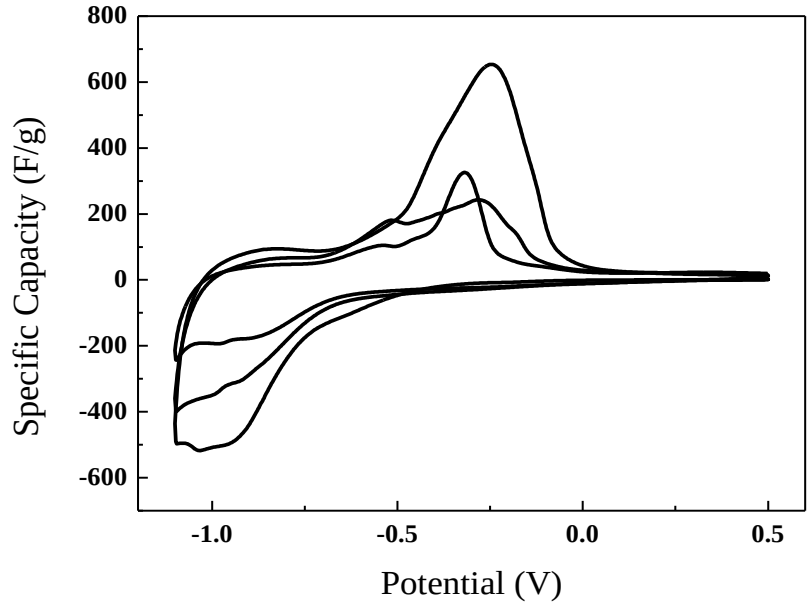

Figure 36 - CV of Fe-Trz-ST1 with 1.0 M Li_2SO_4 of the first 3 cycles

4.4.2 Electrochemical Characterization of Fe-Trz-ST1-V240

This electrode was also tested with 1.0 M Na_2SO_3. The voltage window of 1 V from -0.6 V to 0.4 V has a capacity of 94 F/g (Figure 37). Most of the capacitance is attributed to reversible redox reactions. Low capacitance is due to the nano-rods not having a porous structure.

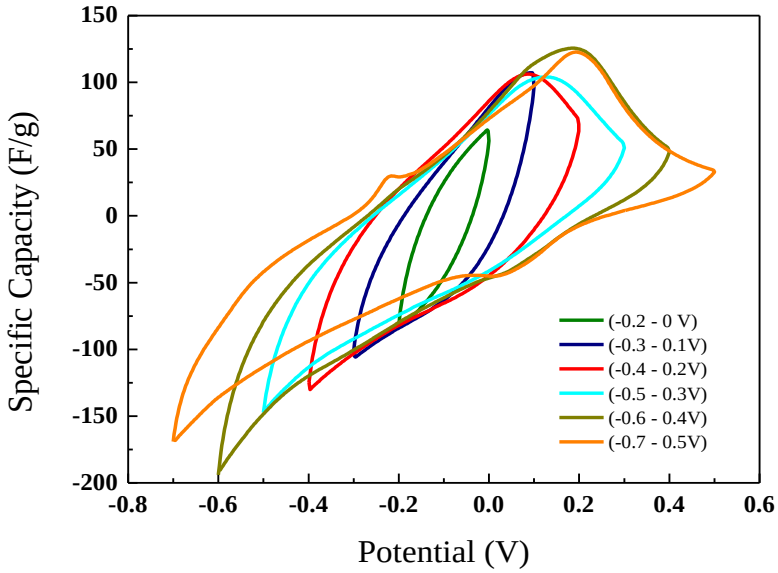

Figure 37 - CV of Fe-Trz-ST1 with 1.0 M Na_2SO_3 with different voltage windows

5 Conclusions and Future Perspectives

This project investigated the synthesis, characterization and performance of four different materials for electrodes in supercapacitors. ZIF-8, Fe-MeIm-ST1, Fe-MeIm-ST2 and Fe-Trz-ST1.

First, ZIF-8 was synthesized and tested to compare performance to that in literature. Morphology of the synthesized ZIF-8 was different from those found in literature forming interlinked, rather than separate particles. Nitrogen containing carbons derived from ZIF-8-C800 had EDLC performance with a capacitance of 156 F/g and voltage window of 1.7 V when tested with lithium sulphate electrolyte.

Synthesizing a ferrous ZIF was not possible, the result of this synthesis was an Iron oxide material with carbon framework, Fe-MeIm-ST1. XRD showed a crystalline structure which was not identified and was composed of an agglomeration of particles as seen in SEM images. After calcination of the material at 800 °C, the electrode with Fe-MeIm-ST1-C800 as an active material showed low capacitance with redox reactions at voltages lower than -0.1 V.

Changing the iron precursor from ferrous chloride to ferrous sulphate changed the morphology of the material (Fe-MeIm-ST2), forming hollow particles, composed of aggregates of smaller particles. After calcination of the material at 300 °C under vacuum, Fe-MeIm-ST2-V300 showed better capacitance. This was achieved by using a 1.0 M sodium sulphite electrolyte due to increased pseudocapacitance. Of the new materials synthesized Fe-MeIm-ST2-V300 showed the best result.

Fe-Trz-ST1 nano-rods were synthesized from ferrous chloride and 1,2,4-Triazole. This material did not have a microporous structure. Calcination above 300 °C led to the formation of tetragonal iron oxide crystalline particles, similar to Fe-Trz-ST1-V600. Fe-Trz-ST1-V600 was tested with a 1.0 M lithium sulphate electrolyte, which did not have stable cycling. Fe-Trz-ST1-V240, kept the nano-rod morphology and when tested with 1.0 M sodium sulphite it had a capacity of 94 F/g with a 1 V voltage window.

Future perspectives are to improve upon these MOFs. The next stage would be to produce a ferrous ZIF, possibly by synthesizing it in an oxygen free environment and to see if this enhances its performance as an electrode material. Further work needs to be carried out to increase the stability of these new materials so that their structures are not affected by the redox reactions. Testing these materials in different electrolytes may also improve their performance.

In order to provide cheap and efficient energy storage devices to satisfy the demand, new electrode materials need to be synthesized and carefully evaluated. They would need to

combine high surface area, adequate pore-size and good electrical conductivity for better supercapacitors.

Bibliography

[1] A. González, E. Goikole, J. A. Barrena e R. Mysyk, "Review on supercapacitors: Technologies and materials," *Renewable and Sustainable Energy Reviews,* vol. 58, pp. 1189-1206, 2016.

[2] H. Chen, T. N. Cong, W. Yang, C. Tan, Y. Li e Y. Ding, "Progress in electrical energy storage system: A critical review," *Progress in Natural Sciences,* vol. 19, pp. 291-312, 2009.

[3] P. Simon, Y. Gogotsi e B. Dunn, "Where Do Batteries End and Supercapacitors Begin?," *Science,* vol. 343, pp. 1210-1211, 2014.

[4] P. S. John R. Miller, "Electrochemical capacitors for energy management," *Science,* vol. 321, pp. 651-652, 2008.

[5] A. G. Pandolfo e A. F. Hollenkamp, "Carbon properties and their role in supercapacitors," *Journal of Power Sources,* vol. 157, p. 11–27, 2006.

[6] E. Frackowiaka e F. Béguinb, "Carbon materials for the electrochemical storage of energy in capacitors," *Carbon,* vol. 39, pp. 937-950, 2000.

[7] O. Yaghi e H. Li, "Hydrothermal Synthesis of a Metal-Organic Framework Containing Large Rectangular Channels," *Journal of the American Chemistry Society,* vol. 117, p. 10401–10402, 1995.

[8] L. Wang, Y. Han, X. Feng e B. Wang, "Metal–organic frameworks for energy storage: Batteries and supercapacitors," *Coordination Chemistry Reviews,* vol. 307, pp. 361-381, 2016.

[9] H. Furukawa, K. E. Cordova, M. O'Keeffe e O. M. Yaghi, "The Chemistry and Applications of Metal-Organic Frameworks," *Science,* vol. 341, p. 974, 2013.

[10] X. Luo, J. Wang, M. Dooner e J. Clarke, "Overview of current development in electrical energy storage technologies and the application potential in power system operation," *Applied Energy,* vol. 137, pp. 511-536, 2015.

[11] F. Lin, X. Dai, Z. Xu, J. Li e Z. Zhao, "High density capacitors," *High Power Laser and Particle Beams,* vol. 1, pp. 94-96, 2003.

[12] R. Kötz e M. Carlen, "Principles and applications of electrochemical capacitors," *Electrochimica Acta,* vol. 45, pp. 2483-2498, 2000.

[13] P. Simon e Y. Gogotsi, "Materials for electrochemical capacitors," *Nature Materials,* vol. 7, pp. 845-854, 2008.

[14] M. C. R Kotz, "Principles and applications of electrochemical capacitors," *Electrochim.,* Vols. %1 de %215-16, pp. 2483-2498, 2000.

[15] S. Kondrat, C. R. Pérez, V. Presser, Y. Gogotsi e A. Kornyshev, "Effect of pore size and its dispersity on the energy storage in nanoporous," *Energy and Environmental Science,* Vols. %1 de %26474-6479, p. 5, 2012.

[16] M. A. Nasalevich, M. v. d. Veen, F. Kapteijn e J. Gascon, "Metal–organic frameworks as heterogeneous photocatalysts: advantages and challenges," *CrystEngComm,* vol. 16, pp. 4919-4926, 2014.

[17] L. Sun, C. H. Hendon, S. S. Park, Y. Tulchinsky, R. Wan, F. Wang, A. Walshbc e M. Dincă, "Is iron unique in promoting electrical conductivity in MOFs?," *Chemical Science,* vol. 6, pp. 4450-4457, 2017.

[18] R. Banerjee, A. Phan, B. Wang, C. Knobler, H. Furukawa, M. O'Keeffe e O. M. Yaghi, "High-throughput synthesis of zeolitic imidazolate frameworks and application to CO2 capture," *Science,* vol. 319, pp. 939-943, 2008.

[19] H.-L. Jiang, B. Liu, Y.-Q. Lan, K. Kuratani, T. Akita, H. Shioyama, F. Zong e Q. Xu, "From metal-organic framework to nanoporous carbon: toward a very high surface area and hydrogen uptake.," *Journal of the American Chemical Society,* vol. 133, pp. 11854-11857, 2011.

[20] J. Tang, R. R. Salunkhe, J. Liu, N. L. Torad, M. Imura, S. Furukawa e Y. Yamauchi, "Thermal Conversion of Core–Shell Metal–Organic Frameworks: A New Method for Selectively Functionalized Nanoporous Hybrid Carbon," *Journal of the American Chemical Society,* vol. 137, pp. 1572-1580, 2015.

[21] Y. Pan, Y. Liu, G. Zeng, L. Zhao e Z. Lai, "Rapid synthesis of zeolitic imidazolate framework-8 (ZIF-8) nanocrystals in an aqueous system," *Chem. Commun.,* vol. 47, pp. 2071-2073, 2011.

[22] S. Brunauer, P. H. Emmett e E. Teller, "Adsorption of Gases in Multimolecular Layers," *Journal of the American Chemical Society,* 1938.

[23] K. S. Park, Z. Ni, A. P. Côté, J. Y. Choi, R. Huang, F. J. Uribe-Romo, H. K. Chae, M. O'Keeffe e O. M. Yaghi, "Exceptional chemical and thermal stability of zeolitic imidazolate frameworks.," *Proceedings of the National Academy of Sciences of the United States of America,* vol. 103, pp. 10186-10191, 2006.

[24] H. Okudera, K. Kihara e T. Matsumoto, "Temperature Dependence of Structure Parameters in Natural Magnetite: Single Crystal X-Ray studies from 126 to 773 K," *Acta Cryst.,* vol. B52, pp. 450-457, 1996.

[25] S.-Y. Wang, K.-C. Ho, S.-L. Kuo e N.-L. Wu, "Investigation on Capacitance Mechanisms of Fe3O4 Electrochemical Capacitors," *Journal of the Electrochemical Society,* vol. 163, 2006.

[26] N.-L. Wu e S.-Y. Wang, "Insight into Pseudocapacitance Mechanism for Fe3O4/Sulfite Supercapacitor," *The Electrochemical Society*.

[27] G. Wang, L. Zhang e J. Zhangb, "A review of electrode materials for electrochemical supercapacitors," vol. 41, pp. 797-828, 2012.